Supplementary Information

Rational design of the single transition-metal atoms anchored on $PtSe_2$ monolayer as the bifunctional OER/ORR electrocatalysts: the defect chemistry and machine learning study

Shijiao Yue[a], Dongying Li[b], Aodi Zhang[a], Yuli Yan[a], Hongxia Yan[c], Zhenzhen Feng[a]*, Wentao Wang[b]*

[a]Institute for Computational Materials Science, School of Physics and Electronics, International Joint Research Laboratory of New Energy Materials and Devices of Henan Province, Henan University, Kaifeng 475004, China.

[b]Guizhou Provincial Key Laboratory of Computational Nano-Material Science, Guizhou Education University, Guiyang 550018, China

[c]College of Sciences, Shihezi University, Shihezi, Xinjiang 832003, China

E-mail: zzfeng@henu.edu.cn; wuli8@163.com

Note S1. Formation energy of the defects

The defect formation energy $E_f(q)$ in the charge state q is calculated by[1, 2]

$$E_f(q) = E_{tot}^{def}(q) - E_{tot}^{pri} - \sum \Delta n_i \mu_i + q(E_{VBM} + E_F) + E_{corr} \quad \text{(S1)}$$

$E_{tot}^{def}(q)$ and E_{tot}^{pri} are the total energies of the supercell with a defect in the charge state q and the pristine supercell of the same size, respectively. The μ_i is the chemical potential of chemical species i (i = Ti, V, Cr, Mn, Fe, Co, Ni, Cu, Ru, Rh, Pd, and Ag). A more in-depth examination of the chemical potential is available in **Note S2**. The number of chemical species i that have been added to ($n_i > 0$) or removed from ($n_i < 0$) the supercell to generate the defect is denoted by n_i. As a convention, E_F is the Fermi level referenced to the valence-band maximum (VBM) in bulk, varying between 0 and the band gap E_g. The E_{VBM} is defined as the energy difference between the pure host (q = 0) and the host with one hole (q = +1) in the valence band of the dilute hole gas limit [3]. E_{corr} is the electrostatic correction for the charged defects due to the finite size of the supercell. The uniformly scaled supercell size technique, in which the lateral lengths are equal ($L_x = L_y = L_z$, refer to **Fig. S1**), is employed to minimize the spurious Coulomb interactions.[4] $E_{corr} = 0$ when this proper procedure is used. This method has been used successfully to investigate the defect formation energy of several 2D materials[4-10]. We use Pt vacancy in −1 charge state defect in $PtSe_2$ supercell as an example to examine the effect of supercell sizes on the periodic defect formation energy (**Fig. S1bc**). Our results show that the defect formation energy converges quite well at the supercell size of 7 × 7 × 1 (Lx = Ly = Lz =26.23 Å). Thus, for all calculations, we used a supercell

size of 7 × 7 × 1 (containing 149 atoms). Correspondingly, the vacuum layer in this supercell is 26.23 Å, which can effectively avoid the periodic interactions along the vacuum direction.

Note S2. The chemical potentials

The chemical potentials of Pt and Se in $PtSe_2$ are not arbitrary but subject to thermodynamic constraints. Under the condition of thermal equilibrium growth, it should be satisfied with the following equation for the case of pure $PtSe_2$:

$$\mu_{Pt} + 2\mu_{Se} = \mu_{PtSe2} \quad \text{(S2)}$$

where μ_{Pt} and μ_{Se} represent the chemical potentials of Pt and Se, μ_{PtSe2} is the chemical potential of $PtSe_2$. Under the same condition, E_{PtSe2} could be expressed as

$$E_{PtSe2} = E_{Pt} + 2E_{Se} + \Delta H_f(PtSe_2) \quad \text{(S3)}$$

where $\Delta H_f(PtSe_2)$ is the formation enthalpy of $PtSe_2$, E_{PtSe2} is the total energy of the $PtSe_2$ per formula unit. E_{Pt} is a reference to the energy of a Pt atom in the cubic Pt[11]. E_{Se} refers to the energy of a Se atom in the monoclinic Se[12]. From **eqn. S3**, accordingly, it follows that

$$\Delta H_f(PtSe_2) = E_{PtSe2} - E_{Pt} - 2E_{Se} \quad \text{(S4)}$$

Under thermal equilibrium growth conditions, $\mu_{PtSe2} = E_{PtSe2}$. That is,

$$\mu_{Pt} + 2\mu_{Se} = E_{Pt} + 2E_{Se} + \Delta H_f(PtSe_2) \quad \text{(S5)}$$

$$\Delta H_f(PtSe_2) = (\mu_{Pt} - E_{Pt}) + 2(\mu_{Se} - E_{Se}) = \Delta\mu_{Pt} + 2\Delta\mu_{Se} \quad \text{(S6)}$$

where $\Delta\mu_{Pt} = (\mu_{Pt} - E_{Pt})$ and $\Delta\mu_{Se} = (\mu_{Se} - E_{Se})$ are defined as the chemical potential changes referenced to the elemental bulk/gaseous state, depending on the growth environments.

The chemical potential of the anchored TM needs to meet the constraints to avoid the formation of related phases.[13-15] For Ti, V, Cr, Mn, Fe, Co, Ni, Cu, Ru, Rh, Pd, and Ag anchored on the $PtSe_2$ monolayer, the experimental lattice constants of impurity-related phases used for the PBE functional calculations are summarized in **Table S1**. The PBE calculated formation enthalpy (given per formula unit) for the impurity-related phases are shown in **Table S2,** together with the Oqmd [16, 17] (the Open Quantum Materials Database will be freely available for public use at https://oqmd.org/) values. It is found that the calculated values are in good agreement with the Oqmd ones.

We take Ti doping as an example for obtaining the chemical potential μ_i in Eqs. S1(i= Ti, V, Cr, Mn, Fe, Co, Ni, Cu, Ru, Rh, Pd, and Ag). The upper bound is $\Delta\mu_{Ti} \leq 0$ as, at this point, precipitation of element Ti to its standard state occurs. Thereby, the

non-formation of the pure solids Ti requires

$$\Delta\mu_{\mathrm{Ti}} < 0 \tag{S7}$$

The following relationships should be satisfied to avoid the formation of other impurity-related phases (such as TiSe and $TiSe_2$):

$$\Delta\mu_{\mathrm{Ti}} + \Delta\mu_{\mathrm{Se}} < \Delta H_{\mathrm{f}}(\mathrm{TiSe}) \tag{S8}$$

$$\Delta\mu_{\mathrm{Ti}} + 2\Delta\mu_{\mathrm{Se}} < \Delta H_{\mathrm{f}}(\mathrm{TiSe_2}) \tag{S9}$$

The maximal Ti chemical potential that satisfies these three equations (**Eqs. S7-S9**) is used in the following calculations. The chemical potential of Ti, V, Cr, Mn, Fe, Co, Ni, Cu, Ru, Rh, Pd, and Ag under the Pt-rich and Se-rich environments calculated by PBE are shown in **Table S3**.

Note S3. Computational hydrogen electrode

The OER performance on the TM@$PtSe_2$ system can be investigated with the widely reported four intermediate steps. For the first step, an H_2O molecular is captured by TM@ $PtSe_2$ substrate from the solvent. It will release a pair of protons and electrons, causing the formation of *OH. Then, the proton and electron pair continuously separate from the *OH, forming an isolate *O. Next, another H_2O molecule in the solvent joins in the reaction with *O randomly to form an *OOH by releasing another pair of proton and electron. Finally, as one proton and electron pair releases again from *OOH, one O_2 molecule is generated, resulting in the reaction loop's termination. The four elementary steps can be described as following equations:

$$2H_2O\,(l) + * \rightarrow *OH + H^{\bullet} + H_2O\,(l) + e' \tag{S10-a}$$

$$*OH + H_2O\,(l) \rightarrow *O + H_2O\,(l) + H^{\bullet} + e' \tag{S10-b}$$

$$H_2O\,(l) + *O \rightarrow *OOH + H^{\bullet} + e' \tag{S10-c}$$

$$*OOH \rightarrow O_2\,(g) + * + H^{\bullet} + e' \tag{S10-d}$$

where *, $H^{\bullet}$, e′ denotes TM@ $PtSe_2$ substrate, proton and electron, respectively. Herein, the energy of O_2 gas is obtained from the experimental reaction energy of $2H_2O \rightarrow 2H_2+O_2$ (4.92eV). Moreover, the energy of ($H^{\bullet}$+e′) pair can be substituted by half of the H_2 molecular at 298 K. Accordingly, the Gibbs free energy change of each step can be described as

$$\Delta G_1 = \Delta G_{*OH} - eU + \Delta G_{H^{\bullet}}(pH) \tag{S11-a}$$

$$\Delta G_2 = \Delta G_{*O} - \Delta G_{*OH} - eU + \Delta G_{H^{\bullet}}(pH) \tag{S11-b}$$

$$\Delta G_3 = \Delta G_{*OOH} - \Delta G_{*O} - eU + \Delta G_{H^{\bullet}}(pH) \tag{S11-c}$$

$$\Delta G_4 = 4.92 - \Delta G_{*OOH} - eU + \Delta G_{H^{\bullet}}(pH) \tag{S11-d}$$

where ΔG_{*OH}, ΔG_{*O}, and ΔG_{*OOH} represent the Gibbs free energy change of *OH, *O, and *OOH intermediate, respectively.

To compute the free energy change (ΔG) of each elementary step of electrochemical urea synthesis, we adopted the computational hydrogen electrode (CHE) model developed by Nørskov et al., according to which the ΔG of an electrochemical reaction is defined as:

$$\Delta G = \Delta E_{DFT} + \Delta ZPE - T\Delta S \quad \text{(S12)}$$

ΔE_{DFT}, ΔZPE, TΔS represent the energy calculated from VASP, zero-point energy, temperature, and entropy correction, and the ΔZPE and TΔS of adsorbed species are listed in **Table S4**. U is the potential measured against a normal hydrogen electrode (NHE) at standard conditions (T = 298.15 K, P = 1 bar, pH = 0). The free energy change of the protons relative to the NHE at non-zero pH is described by the Nernst equation as $\Delta G_{H^\bullet}(pH) = -k_B T \ln(10) \times pH$.

The energy differences of the corresponding intermediates are expressed as:

$$\Delta E_{DFT}(*OH) = E_{DFT}(*OH) - E(*) - [E_{DFT}(H_2O) - 1/2 * E_{DFT}(H_2)] \quad \text{(S13-a)}$$

$$\Delta E_{DFT}(*O) = E_{DFT}(*O) - E(*) - [E_{DFT}(H_2O) - E_{DFT}(H_2)] \quad \text{(S13-b)}$$

$$\Delta E_{DFT}(*OOH) = E_{DFT}(*OOH) - E(*) - [2 * E_{DFT}(H_2O) - 3/2 * E_{DFT}(H_2)] \quad \text{(S13-c)}$$

where the E_{DFT} (*OH), E_{DFT} (*O), E(*), E_{DFT} (H_2O), and E_{DFT} (H_2) indicate the total energy of *OH, *O, substrate, H_2O molecular, H_2 molecular, separately. The Gibbs free energy (G) of gas O_2 (g), H_2 (g) and liquid water H_2O (l) at 1/0.035 bar and 298.15 K are listed in **Table S5**.

Since the energy of the proton/electron pair is small enough compared to the elemental steps, the corresponding energy is negligible for these processes and is not considered. The maximum energy change among the three steps would determine the reaction rate, i.e., the potential determining steps (PDSs). To describe the catalytic activity, we define the overpotential as:

$$\eta^{OER} = \frac{\max[\Delta G_1, \Delta G_2, \Delta G_3, \Delta G_4]}{e} - 1.23 \quad \text{(S14)}$$

where 1.23 represents the equilibrium potential, η_{OER} is the overpotential of OER, and e is the charge of one electron. Based on previous reports, a lower η value on a given catalyst suggests a less energy input for OER/ORR, thus demonstrating its higher OER/ORR catalytic activity.

Similarly, the overpotential of ORR (η^{ORR}) is defined as:

$$\eta^{ORR} = \frac{\max[-\Delta G_1, -\Delta G_2, -\Delta G_3, -\Delta G_4]}{e} + 1.23 \quad \text{(S15)}$$

Note S4 Machine learning

The coefficient of determination (R^2) and root-mean-square error(RMSE), defined as:

$$R^2=1-\frac{\frac{1}{n}\sum_{i=1}^{n}(y_i-\hat{y}_i)^2}{\frac{1}{n}\sum_{i=1}^{n}(y_i-\mu_i)^2} \quad \text{(S16)}$$

$$RMSE=\sqrt{\frac{1}{n}\sum_{i=1}^{n}(y_i-\hat{y}_i)^2} \quad \text{(S17)}$$

in which y_i and $\hat{y}_i$ are the sample label value and the predicted value, respectively. Usually, a higher R^2 and a lower RMSE means a more precise ML model.

a. The computational method of the GBR regression algorithm

The **Gradient Boosted Regression (GBR)** model is an integrated ML algorithm that is generated by the integration of weak regression trees[18, 19]. Given the training samples $\boldsymbol{D} = \{(\mathbf{x_1}, \mathbf{y_1}), (\mathbf{x_2}, \mathbf{y_2}) \ldots, (\mathbf{x_n}, \mathbf{y_n})\}$, the number of leaf nodes in every regression tree is $\boldsymbol{J}$. We divided the input data into J disjoint areas and defined each regression tree as $\mathbf{t_m(x)}$. The training goal of GBR is to minimize the loss function $\boldsymbol{L}$, and the parameters of decision tree $\boldsymbol{\theta_m}$ are determined through empirical risk minimization:

$$\boldsymbol{\theta_m}=\underset{\boldsymbol{\theta_m}}{\operatorname{argmin}}\sum_{i=1}^{n}\mathbf{L}\left(y_i, f_{(m-1)}(x_i)+\mathbf{t_m}(x_i)\right) \quad \text{(S18)}$$

The process of GBR training is as follows:

(a) Initialize a regression tree function $f_0(x)$.

(b) Train GBR in the gradient decline direction, and compute the negative gradient value of the loss function as the estimated value of the residual. For the m_{th} iteration, GBR generates a regression tree according to the residual and updates the current function $f_m(x)$.

(c) The final regression model is the weighted sum of several weak regression trees, which is defined as:

$$f_M(x)=\sum_{m=1}^{M}t(x,\boldsymbol{\theta_m}) \quad \text{(S19)}$$

b. The computational method of the RFR regression algorithm

The **Random Forest Regression (RFR)** model is an ensemble learning method for regression by constructing a multitude of decision trees at training time and outputting the class that is the mode of the classes (classification) or mean/average prediction (regression) of the individual trees[20]. Random decision forests correct for

decision trees' habit of overfitting to their training set. The training algorithm for random forests applies the general technique of bootstrap aggregating, or bagging, to tree learners. Given a training set $X = x_1 ... x_n$ with responses $Y = y_1 ... y_n$, bagging repeatedly (B times) selects a random sample with replacement of the training set and fits trees to these samples:

(a) For b = 1... B: Sample, with replacement, n training examples from X, Y; call these X_b, Y_b; Train a regression tree f_b on X_b, Y_b.

(b) After training, predictions for unseen samples x' can be made by averaging the predictions from all the individual regression trees on x'

$$\hat{f} = \frac{1}{B} \sum_{b=1}^{B} f_b(x') \quad \text{(S20)}$$

c. The computational method of the SVR regression algorithm

The **Support Vector Regression (SVR)** model is a supervised learning model with associated learning algorithms that analyze data used for regression analysis[21]. Given a set of training examples, each marked as belonging to one or the other of two categories, an SVM training algorithm builds a model that assigns new examples to one category or the other, making it a non-probabilistic binary linear classifier (although methods such as Platt scaling exist to use SVM in a probabilistic classification setting). An SVM model is a representation of the examples as points in space, mapped so that the examples of the separate categories are divided by a clear gap that is as wide as possible. New examples are then mapped into that same space and predicted to belong to a category based on the side of the gap on which they fall. In addition to performing linear classification, SVMs can efficiently perform a non-linear classification using what is called the kernel trick, implicitly mapping their inputs into high-dimensional feature spaces. Training the original SVR to:

(a) Minimize $\frac{1}{2} ||w||^2$.

$$\text{(b) Subject to} \left| y_i - \langle w, x_i \rangle - b \right| \leq \varepsilon \quad \text{(S21)}$$

where x_i is a training sample with a target value y_i. The inner product plus intercept $\langle w, x_i \rangle - b$ is the prediction for that sample, and ε is a free parameter that serves as a threshold: all predictions have to be within a ε range of the true predictions. Slack variables are usually added into the above to allow for errors and to allow approximation in the case the above problem is infeasible.

d. The computational method of the KNR regression algorithm

The ***K*-Neighbour Regression (KNR)** model is a non-parametric method proposed by Thomas Cover used for classification and regression[22]. In both cases, the input consists of the k closest training examples in the feature space. The output depends on whether k-NN is used for classification or regression. In k-NN regression, the output is the property value for the object. This value is the Average of the values of k nearest neighbors.

In the classification phase, *k* is a user-defined constant, and an unlabeled vector (a query or test point) is classified by assigning the label which is most frequent among the k training samples nearest to that query point. A commonly used distance metric for continuous variables is Euclidean distance. For discrete variables, such as for text classification, another metric can be used, such as the overlap metric (or Hamming distance). Often, the classification accuracy of *k*-NN can be improved significantly if the distance metric is learned with specialized algorithms such as Large Margin Nearest Neighbor or Neighborhood components analysis. This algorithm works as follows:

(a) Compute the Euclidean or Mahalanobis distance from the query example to the labeled examples.

(b) Order the labeled examples by increasing distance.

(c) Find a heuristically optimal number k of nearest neighbors, based on RMSE. This is done using cross-validation.

(d) Calculate an inverse distance weighted average with the k-nearest multivariate neighbors.

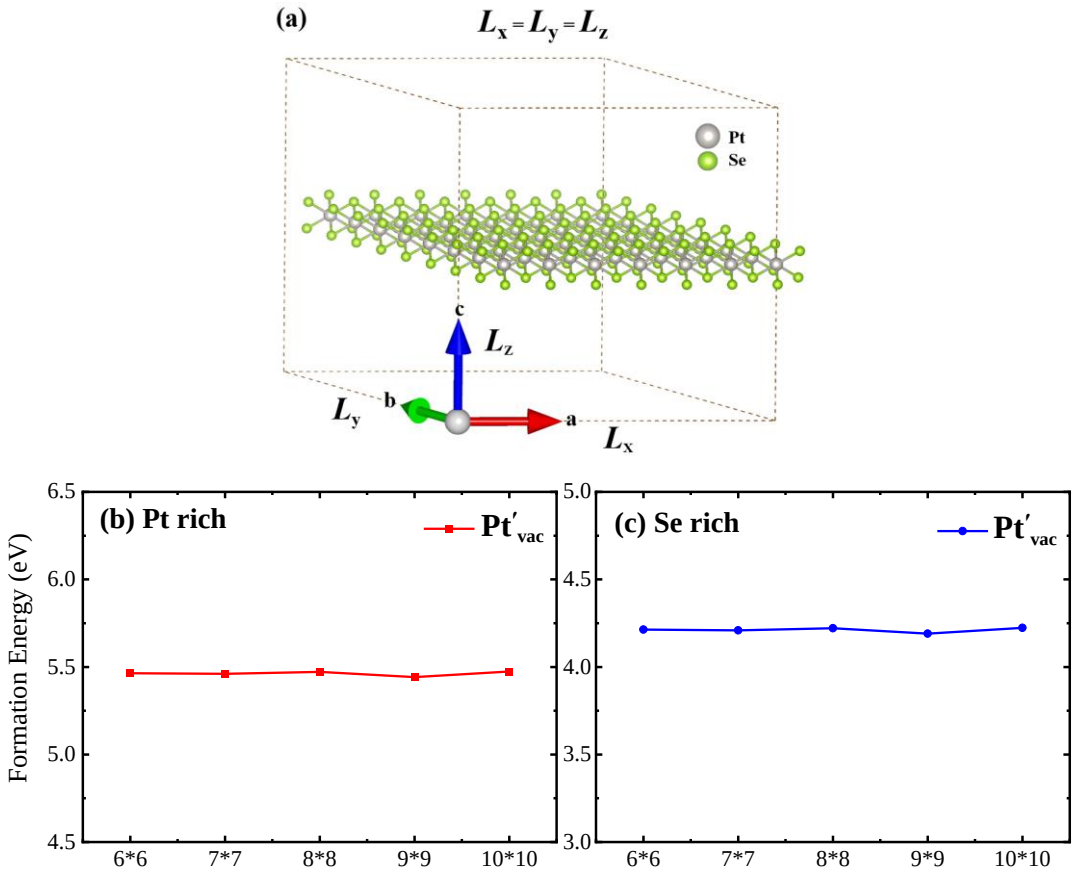

Fig. S1. (a) Uniformly scaled supercell of $PtSe_2$ monolayer with the lateral lengths equal. (b)(c) Convergence of defect (Pt vacancy in $PtSe_2$ in -1 charge state) formation energies as a function of uniformly scaled supercell size in all the directions (lateral length: Lx = Ly = Lz). The bottom x-axis represents the supercell size, which * denotes the cubic supercell size. For example, 6*6 illustrates 6×6 ×1 supercell size. The red and blue lines indicate Pt-rich and Se-rich conditions, respectively.

The formation energy difference for most cases of the different supercell sizes (6×6×1, 7×7×1, 8×8×1, 9×9 ×1, 10×10×1) is only around 0.04 eV, which is consistent with the other theoretical reports[14, 23]. This result demonstrates that the adopted 7×7×1 supercell model (Lx = Ly = Lz =26.23 Å) is acceptable and credible. The formation energy of Pt vacancy of $PtSe_2$ in -1 charge state converged at around 4.2eV under the Se-rich condition, while under the Pt-rich condition, it converged at around 5.47eV. It is found that Se-rich conditions can promote the formation of Pt vacancy due to its lower formation energy.

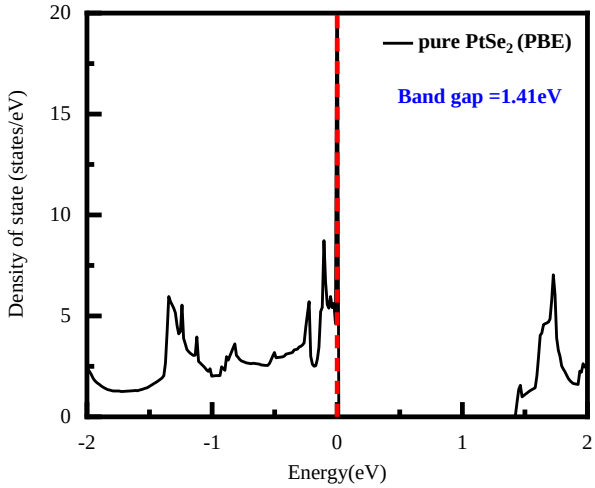

Fig. S2. (a) The total density of state calculated for perfect $PtSe_2$ by PBE functional. The position of the valence band maximum (VBM) is placed at zero. The band gap of monolayer $PtSe_2$ at the PBE level is 1.41eV, which is consistent with other reports[24-27].

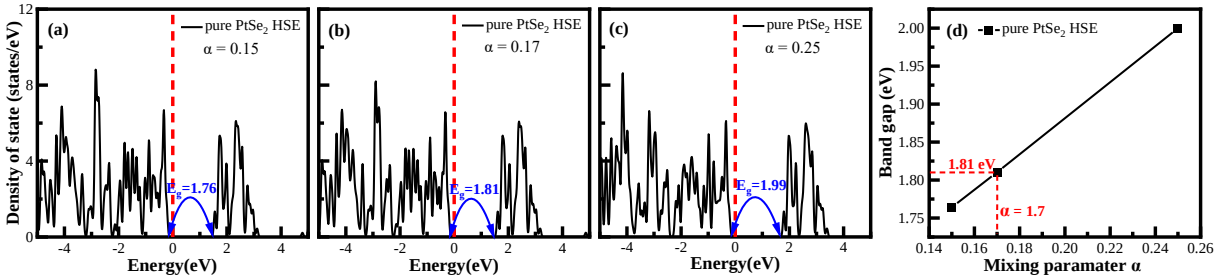

Fig. S3. The total density of states (TDOS) of $PtSe_2$ (unit cell) using the HSE06 method with different Hartree–Fock mixing parameters α, (a) α=0.15, (b) α=0.17, and (c) α= 0.25. The valence band maximum (VBM) position is placed at zero. (d) The bandgap as a function of Hartree–Fock mixing parameters α.

We tested the bandgap of pure $PtSe_2$ by adjusting the Hartree–Fock mixing parameter (α) from 0.15 to 0.25. According to the linear relationship between α and bandgap, when α increases from 0.15 to 0.25, the bandgap increases accordingly from 1.76 eV to 1.99 eV. Especially when α = 0.17, the calculated bandgap is 1.81 eV for pure $PtSe_2$, near the experimental band gap of 1.80 eV.[28]

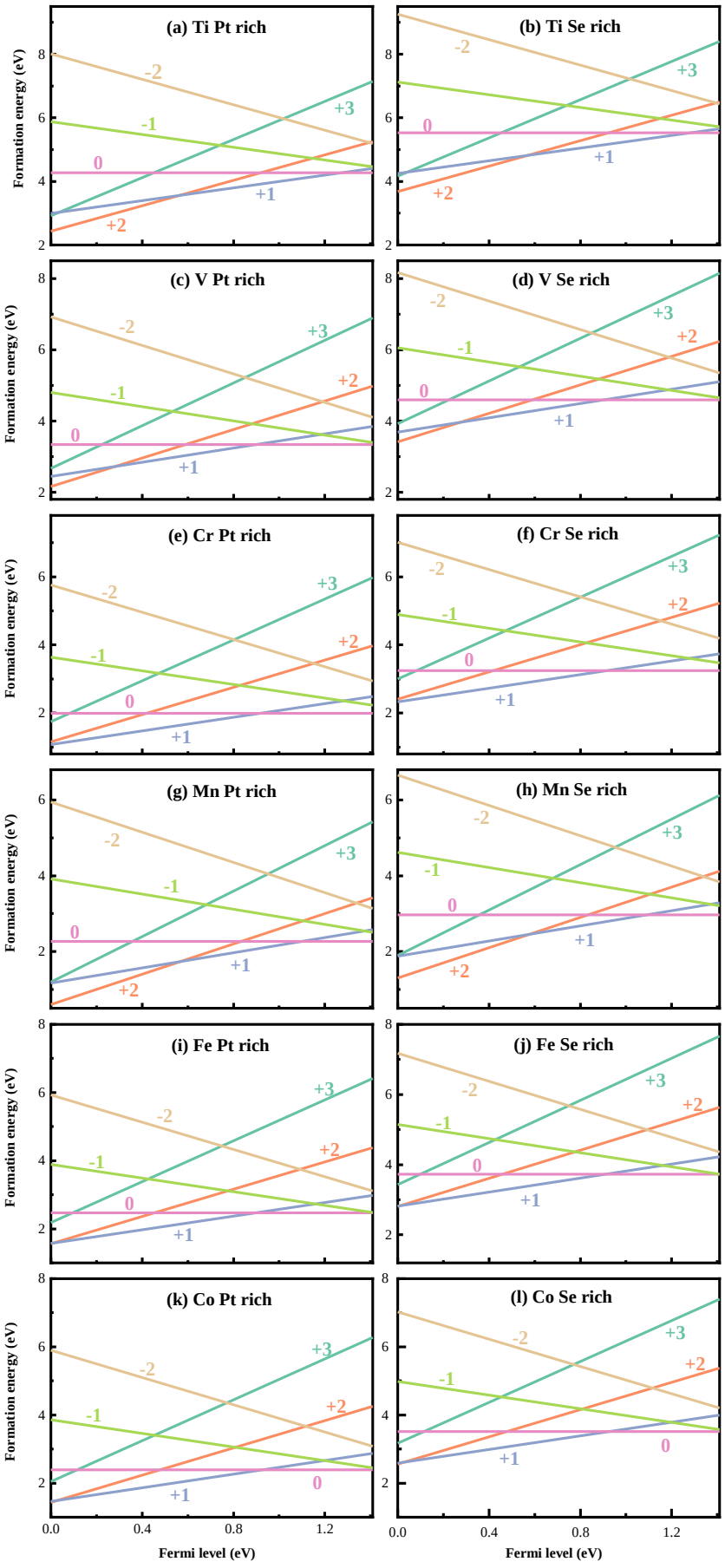
(a) Ti Pt rich
(b) Ti Se rich
(c) V Pt rich
(d) V Se rich
(e) Cr Pt rich
(f) Cr Se rich
(g) Mn Pt rich
(h) Mn Se rich
(i) Fe Pt rich
(j) Fe Se rich
(k) Co Pt rich
(l) Co Se rich
Formation energy (eV)
Fermi level (eV)
-2
-1
0
+1
+2
+3
2
4
6
8
0.0
0.4
0.8
1.2

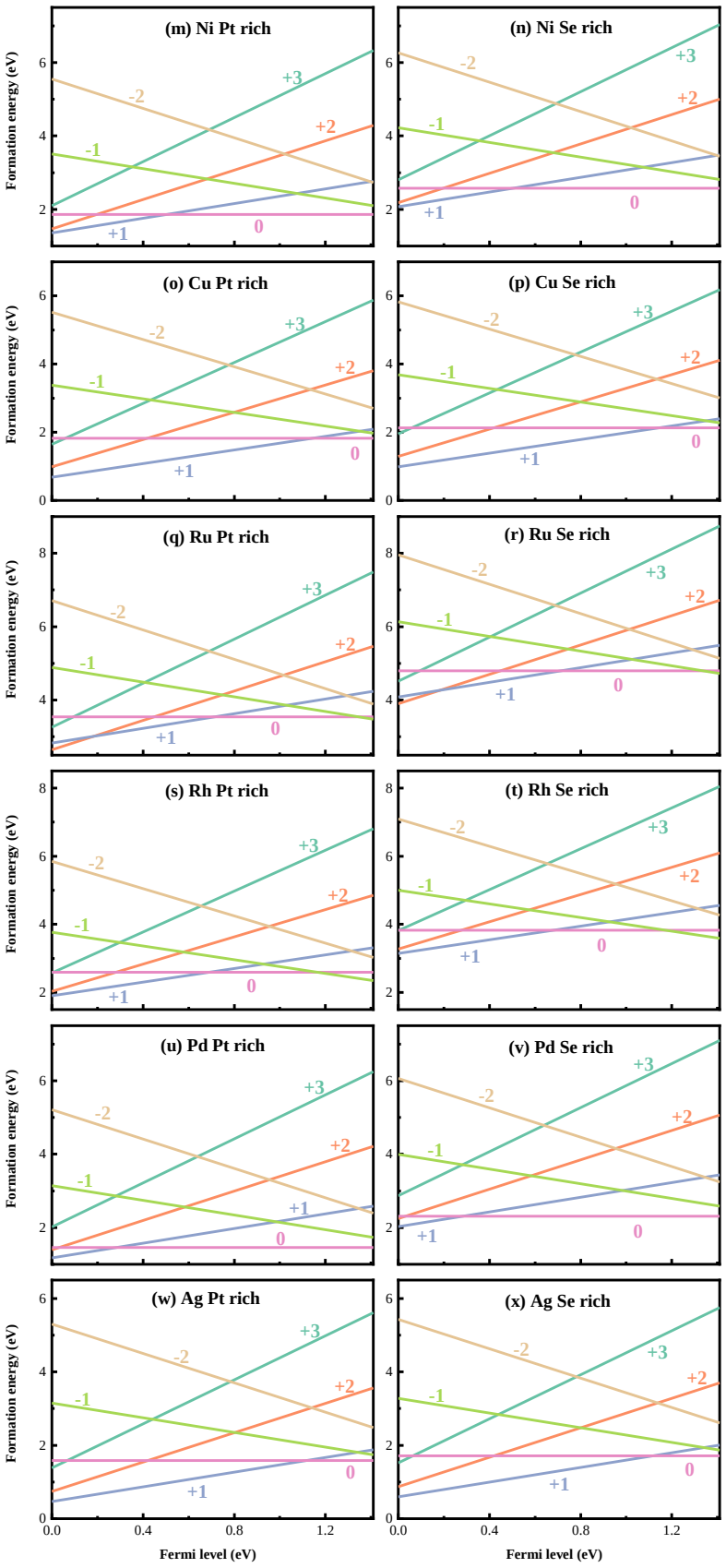

Fig. S4. The formation energies of TM@$PtSe_2$ under Pt-rich and Se-rich conditions are plotted as a function of the Fermi level with respect to the VBM. The Fermi level (E_F) at the VBM and the conduction band minimum (CBM) is set to 0.00 and 1.41 eV, respectively.

In both Pt-rich and Se-rich conditions, the formation energies of TM@$PtSe_2$ in various possible charge states (-3 to +3) as a function of the Fermi level are calculated to examine the convergence of the charge state. The formation energy of the −3 charge state is consistently higher than that of the −2, −1, and 0 charge states when the charge state is negative. Similarly, the formation energy of the +3 charge state surpasses that of the +2, +1, and 0 charge states when the charge state is positive. These findings suggest that the calculated charge states converge, as the unreasonable charge states exhibit relatively higher formation energies.

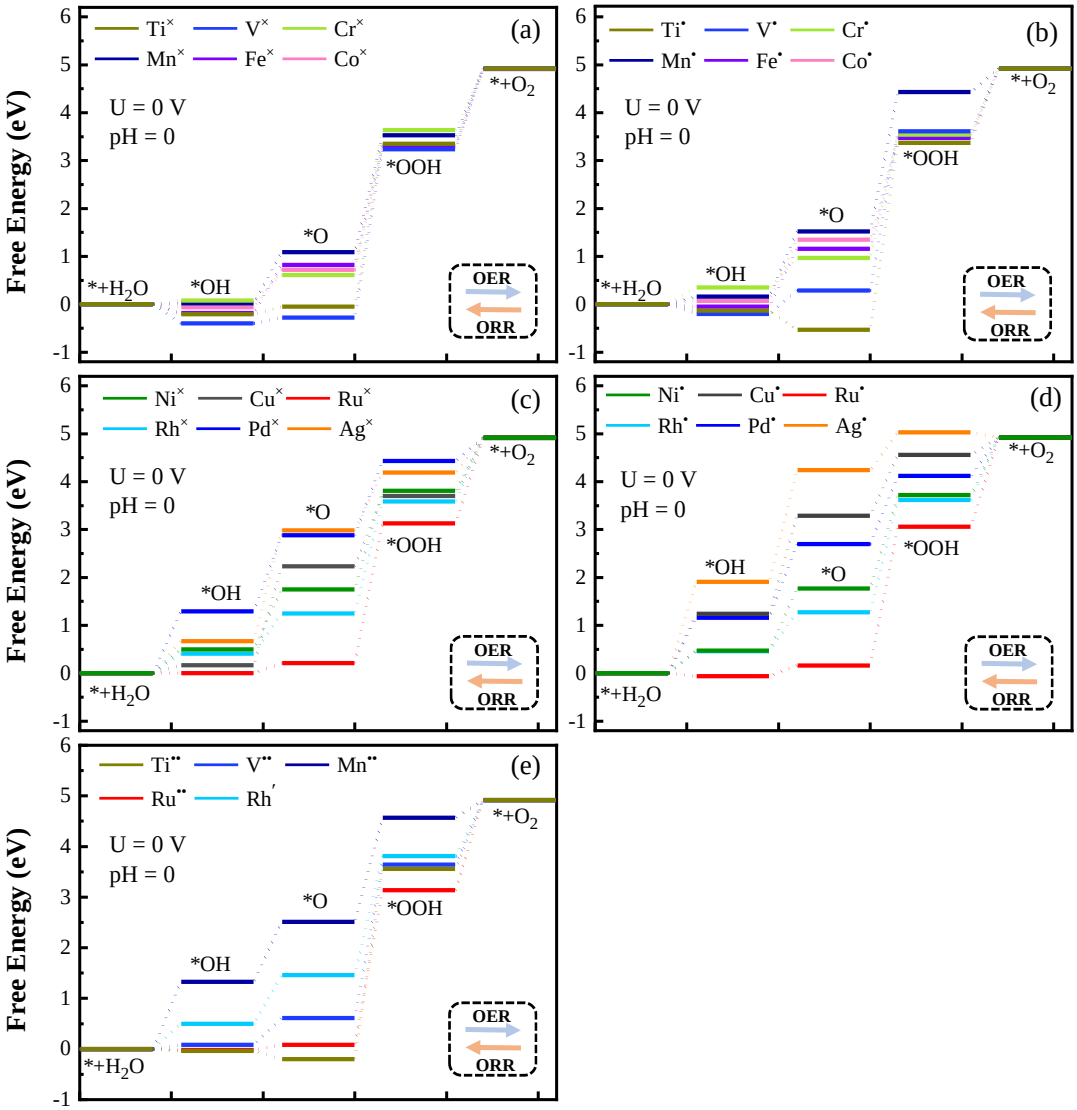

Fig. S5. The energy steps of OER and ORR of TM@$PtSe_2$ system under PH=0 for U = 0 V. The OER reaction process is from left to right, while the ORR is contrary to the OER progress.

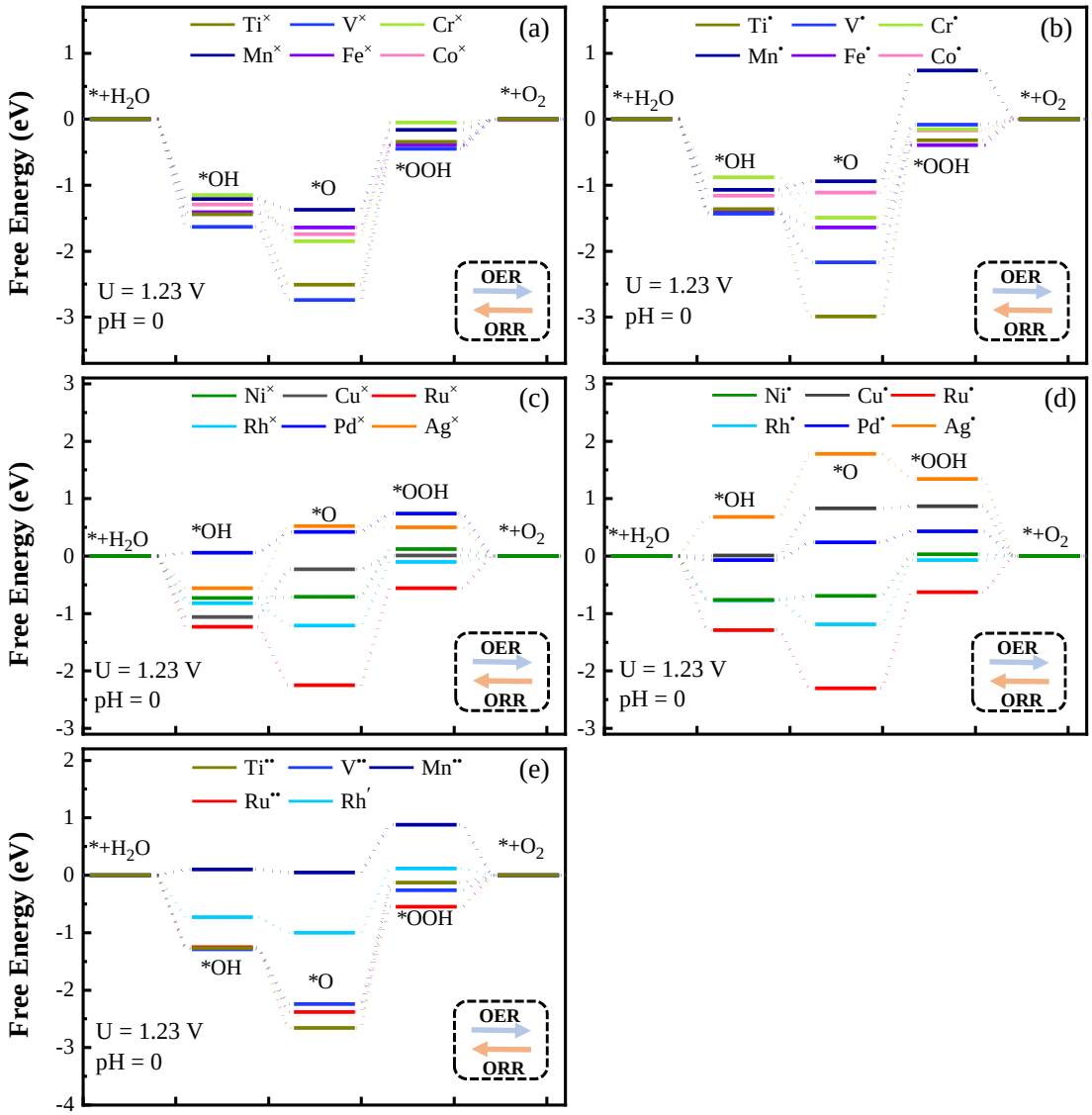

Fig. S6. The energy steps of OER and ORR of TM@$PtSe_2$ system under PH=0 for U = 1.23 V. The OER reaction process is from left to right, while the ORR is contrary to the OER progress.

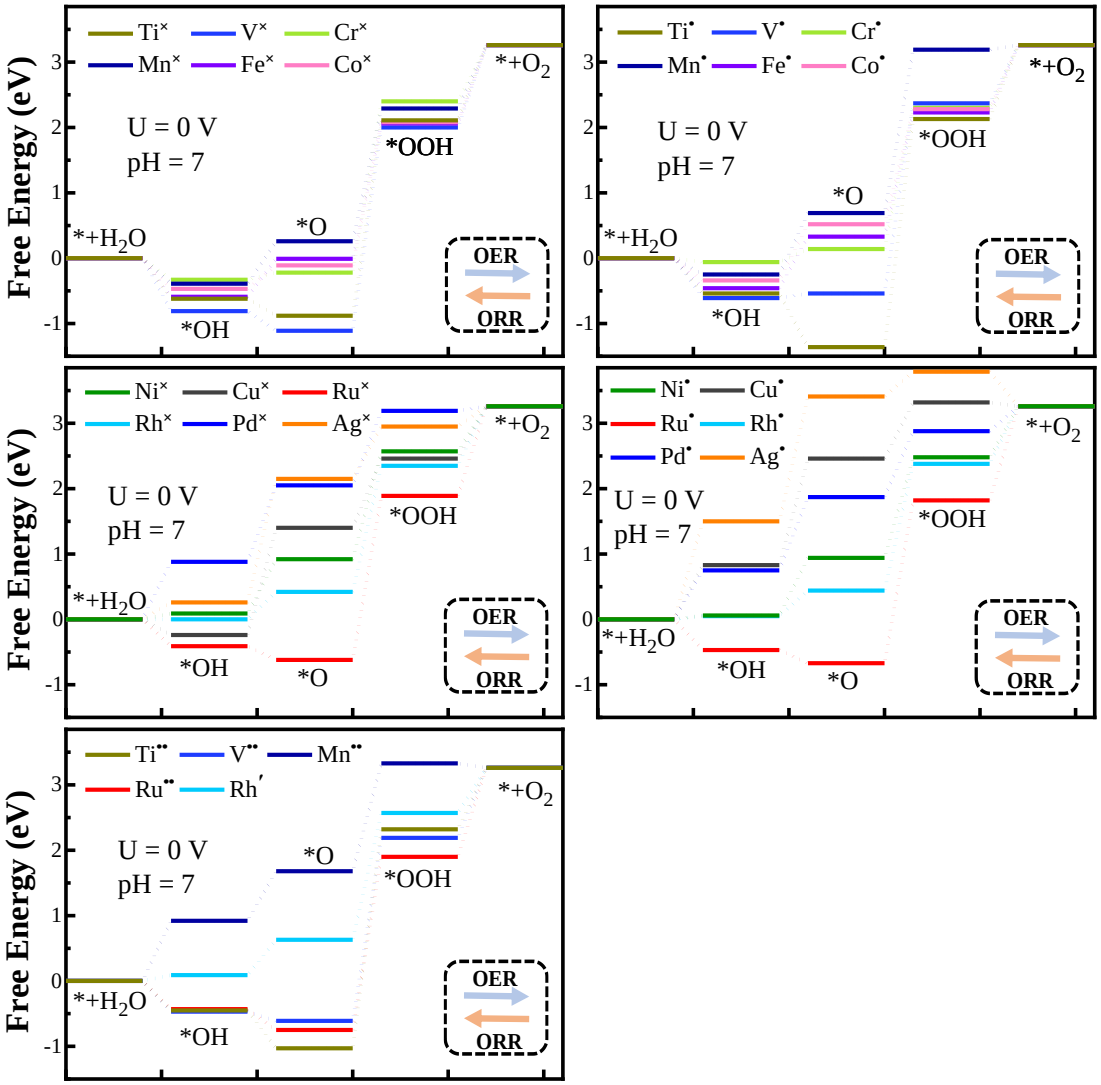

Fig. S7. The energy steps of OER and ORR of TM@$PtSe_2$ system under pH=7 for U = 0 V. The OER reaction process is from left to right, while the ORR is contrary to the OER progress.

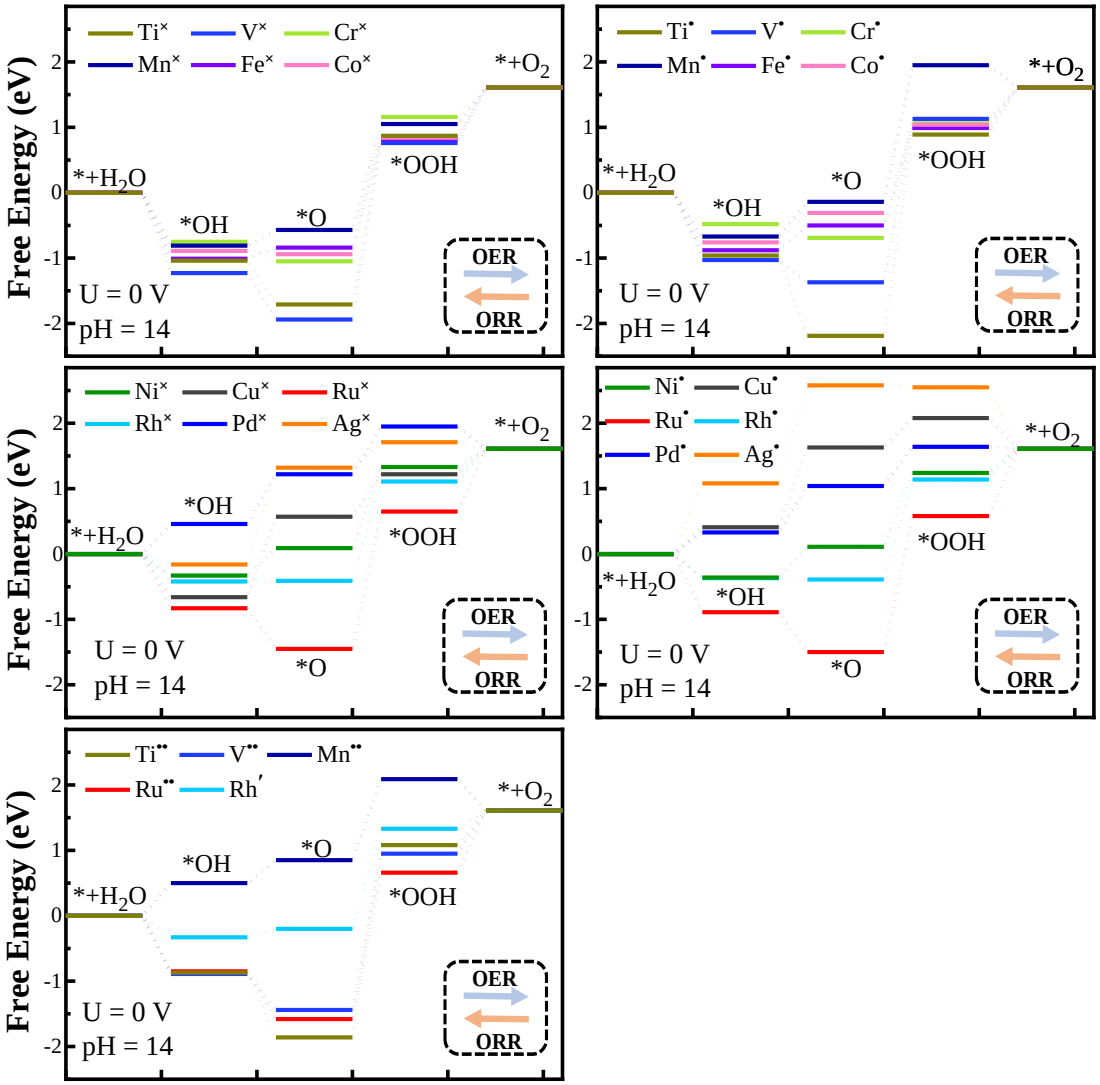

Fig. S8. The energy steps of OER and ORR of TM@$PtSe_2$ system under pH=14 for U = 0 V. The OER reaction process is from left to right, while the ORR is contrary to the OER progress.

In Fig. S5-S8, the OER progress is from left to right (stages of * + H_2O, *OH, *O, *OOH, and *+ O_2, respectively), while the ORR progress is contrary since they are inverse processes of each other. Under U = 0 V (**Fig.S5**), each elementary step of the OER process is uphill, meaning it cannot react spontaneously. Theoretically, when we apply an ideal voltage of 1.23V, each step can undergo spontaneous reactions. However, as shown in **Fig.S6**, it can be observed that many steps are still uphill. In the actual process of OER, some electronic steps need to provide an external voltage higher than 1.23 V due to the influence of catalytic activity.

Furthermore, we elucidate the effects of pH on the free energies of the OER and ORR. The free energy can be obtained via the following equation: $\Delta G = \Delta E + \Delta E_{ZPE} - T\Delta S + \Delta G_{pH} + \Delta G_U$, in which $\Delta G_{pH} = -k_B T \ln(10) \times Ph = 2.303\ k_B T\ pH = 0.05916 \times pH$

(T = 298.15K,). According to this equation, it is clear that the free energy of each net coupled proton and electron transfer step becomes less negative as the pH value increases at U = 0 V. Thus, at pH = 7, the Gibbs free energies of each elemental step in the four basic steps decreased by 0.414 eV, at pH = 14, the Gibbs free energies of each elemental step in the four basic steps decreased by 0.828 eV.

As shown in **Fig. S7** and **Fig. S8**, the overpotential of OER/ORR for each TM@ $PtSe_2$ system is unchanged compared to the case of pH=0. This is because the overpotential (η) of oxygen reactions can be attained by probing the reaction-free energy of the different elementary steps, based on the hypothesis that there are no more barriers from adsorption/ dissociation of O_2 or proton-electron transfer reaction. Since the transfer rate of a solvated proton to adsorbed OH^- through the proton transfer steps shows a negligible barrier, signifying the downhill energy of proton transfer, and most previously reported models neglect the influence of the electric field in the double layer, so the calculated free energy of intermediates displays no difference in alkaline and acidic conditions at fixed potential on the RHE scale[29, 30].

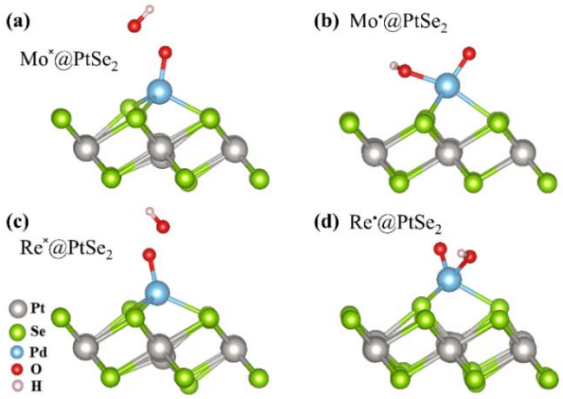

Fig. S9. Optimized structures of *OOH adsorbed on (a) $Mo^{\times}@PtSe_2$, (b) $Mo^{\bullet}@PtSe_2$, (c) $Re^{\times}@PtSe_2$ and (d) $Re^{\bullet}@PtSe_2$.The *OOH radical dissociates on these systems (a stable *OOH adsorption geometrycannot be obtained).

The bifunctional OER/ORR activity of the $Mo^{\times}@PtSe_2$, $Mo^{\bullet}@PtSe_2$, $Re^{\times}@PtSe_2$, and $Re^{\bullet}@PtSe_2$ systems are calculated. However, the absorbed structures of *OH, *O, and *OOH intermediates on these systems are unreasonable. Thus, we can not obtain *OH (ΔG_1), *OH to *O (ΔG_2), *O to *OOH (ΔG_3), *OOH to O_2 (ΔG_4), η^{OER}, and η^{ORR} of $Mo@PtSe_2$ and $Re@PtSe_2$ systems. In the following calculation, we do not consider $Mo@PtSe_2$ and $Re@PtSe_2$ systems.

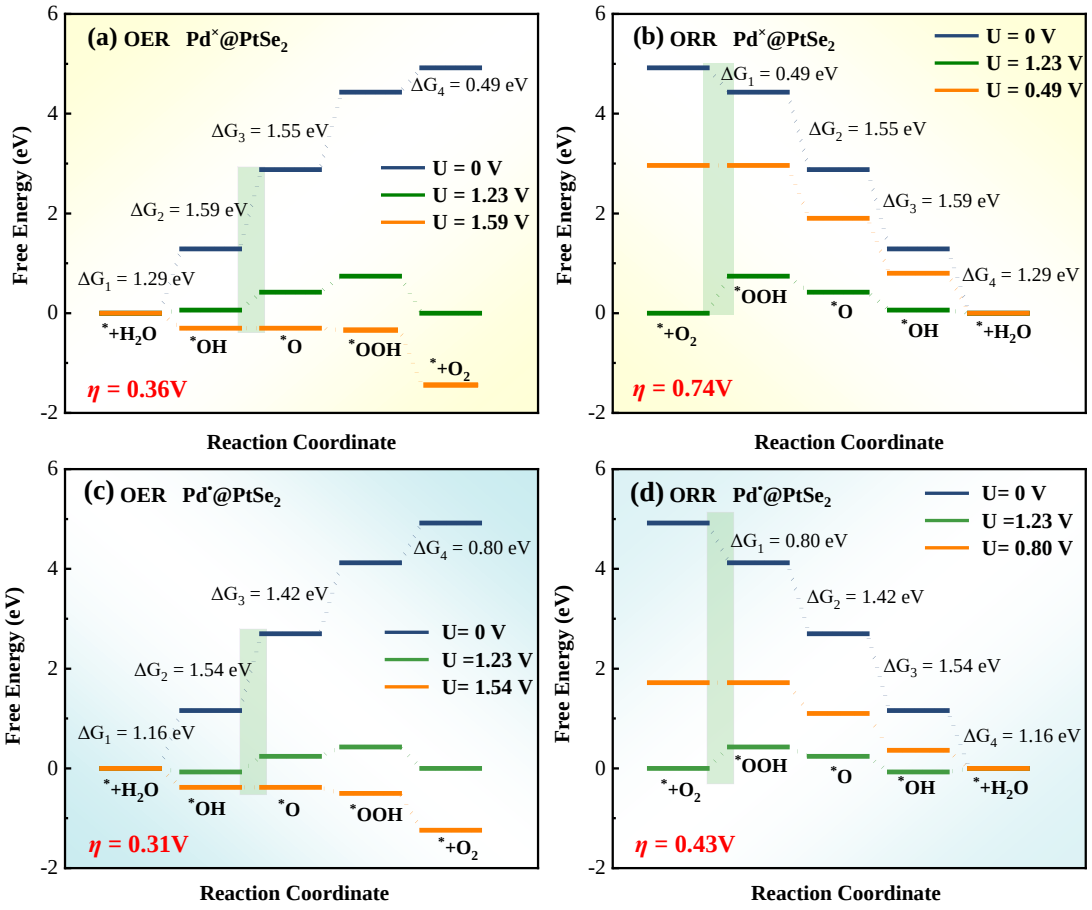

Fig. S10. Free energy pathway plots for the $Pd^{\times}$@$PtSe_2$ ((a) OER and (b) ORR) and $Pd^{\bullet}$@$PtSe_2$ ((c) OER and (d) ORR) at different electrode potentials in an acidic medium. The light green shadow represents the rate-determining steps of OER and ORR. The deep blue and green lines represent U=0V and U=1.23V, respectively. The orange line represents the minimum external voltage required for the system to undergo OER while ensuring spontaneous reactions and the maximum voltage provided to the external environment when ORR occurs.

We further investigated the Gibbs free energy changes of the four reaction steps at $Pd^{\times}$@$PtSe_2$ and $Pd^{\bullet}$@$PtSe_2$ under different potentials. The four steps of OER at $Pd^{\times}$@$PtSe_2$ and $Pd^{\bullet}$@$PtSe_2$ are uphill at U = 0 V as shown in **Fig. S10** (a) and (b), indicating all the four reaction steps are endothermic and are not easy to occur. When U increases to 1.23 V, the second (* + OH converting into *O and $H^{\bullet}$) and third steps (converting * + OOH to O_2) at $Pd^{\times}$@$PtSe_2$ and $Pd^{\bullet}$@$PtSe_2$ still are uphill. The minimum potentials OER proceeds spontaneously under are 1.59 and 1.54 V at $Pd^{\times}$@$PtSe_2$ and $Pd^{\bullet}$@$PtSe_2$, respectively. RuO_2 is regarded as the best OER electrocatalyst with a predicted valid electrode potential of 1.60 V. [31] In comparison, both $Pd^{\times}$@$PtSe_2$ and $Pd^{\bullet}$@$PtSe_2$ have higher catalytic activity for OER compared with RuO_2. As shown in **Fig. S10** (b) and (d), the first and fourth steps of ORR, hydrogenation of * + O_2 to

*OOH and conversion of * + OH to water are uphill at the equilibrium potential (U = 1.23 V) on Pd•@PtSe2. The first step of ORR is uphill on Pd×@PtSe2, showing that ORR will not occur spontaneously at U = 1.23 V. Under zero potential, all four steps of ORR are downhill, meaning that the ORR proceeds spontaneously. The maximum potentials under which ORR occurs spontaneously (valid electrode potentials) on Pd×@PtSe2 and Pd•@PtSe2 are calculated as 1.23 V – η^{ORR}, which are 0.49 and 0.80 V, respectively. The catalyst with better ORR electrocatalytic performance should have a smaller overpotential and a larger valid electrode potential. The valid electrode potential of ORR on Pd•@PtSe2 (0.80 V) is larger than that on Pt (111) surface (0.79 V). [32] Correspondingly, the ORR electrocatalytic performance of Pd•@PtSe2 is better than that of the Pt (111) surface. Our result further demonstrates that Pd×@PtSe2 and Pd•@PtSe2 are promising ORR and OER bifunctional electrocatalysts having higher electrocatalytic activity for OER and ORR than the previously reported OER and ORR catalysts.

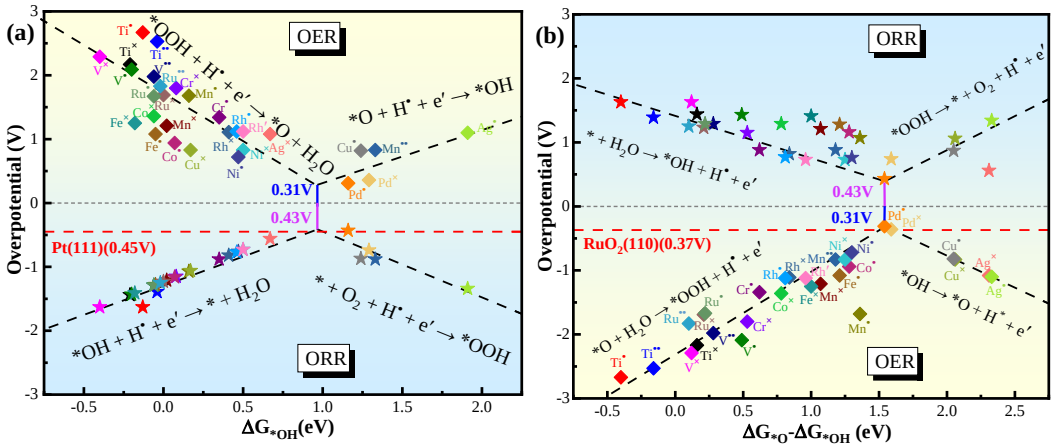

Fig. S11. Dual activity (OER/ORR) volcano maps of TM@PtSe2 for (a) η VS ΔG_{*OH} and (b) η VS ΔG_{*O} - ΔG_{*OH} are presented. The systems at the mountain peak position exhibit the best catalytic performance. The systems located at the dashed line position indicate that the step represented by the dashed line is the RDS for those systems. The mountain peak positions for OER and ORR are consistent, which suggests that the best catalytic for ORR and OER are similar in TM@PtSe2.

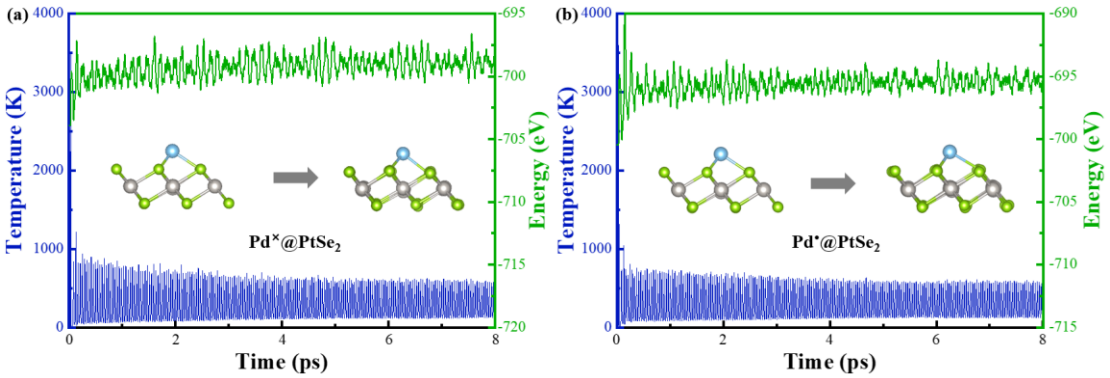

Fig. S12. The evolution of the total energy and temperature per atom within 8 ps at 300K for $Pd^{\times}$@$PtSe_2$ (a) and $Pd^{\bullet}$@$PtSe_2$ (b), the inserted pictures are the atomic structure for initial state and final state of Pd@$PtSe_2$.

$Pd^{\times}$@$PtSe_2$ and $Pd^{\bullet}$@$PtSe_2$, with the best catalytic activity, are selected to perform the AIMD under different temperatures. It is evident from the simulations that the overall frameworks of these systems undergo only minor changes throughout the entire dynamics calculations process. None of the structures exhibit significant structural reconstruction, and they can revert to their initial structures following structural relaxation. This suggests that these systems exhibit robust thermal stability.

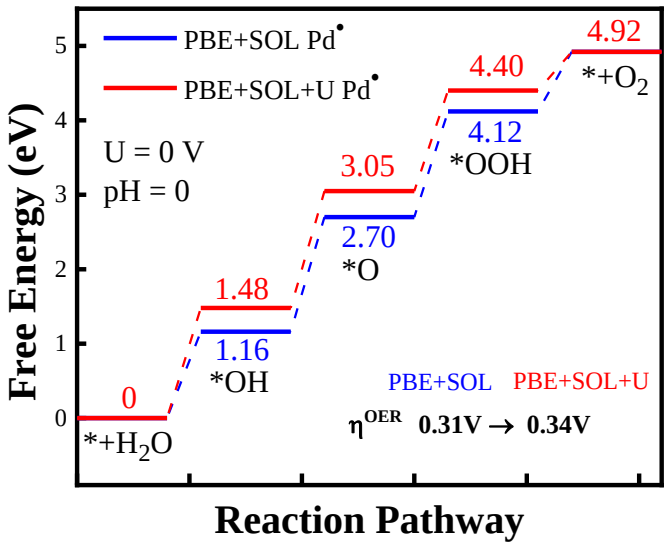

Fig. S13. Gibbs free energy diagrams of $Pd^{\bullet}$@$PtSe_2$ using PBE+SOL calculation and PBE+SOL +U calculation.

The $Pd^{\bullet}$@$PtSe_2$ OER overpotential is 0.34 V for the DFT+U method and 0.31 V for the PBE+SOL method. This indicates that the difference in Gibbs free energy of the four steps calculated by the two methods is relatively small. These results indicate that the PBE+SOL level is sufficient for describing the electrocatalytic activity, and the GGA+U method has negligible impact, consistent with previous studies.[33-37]

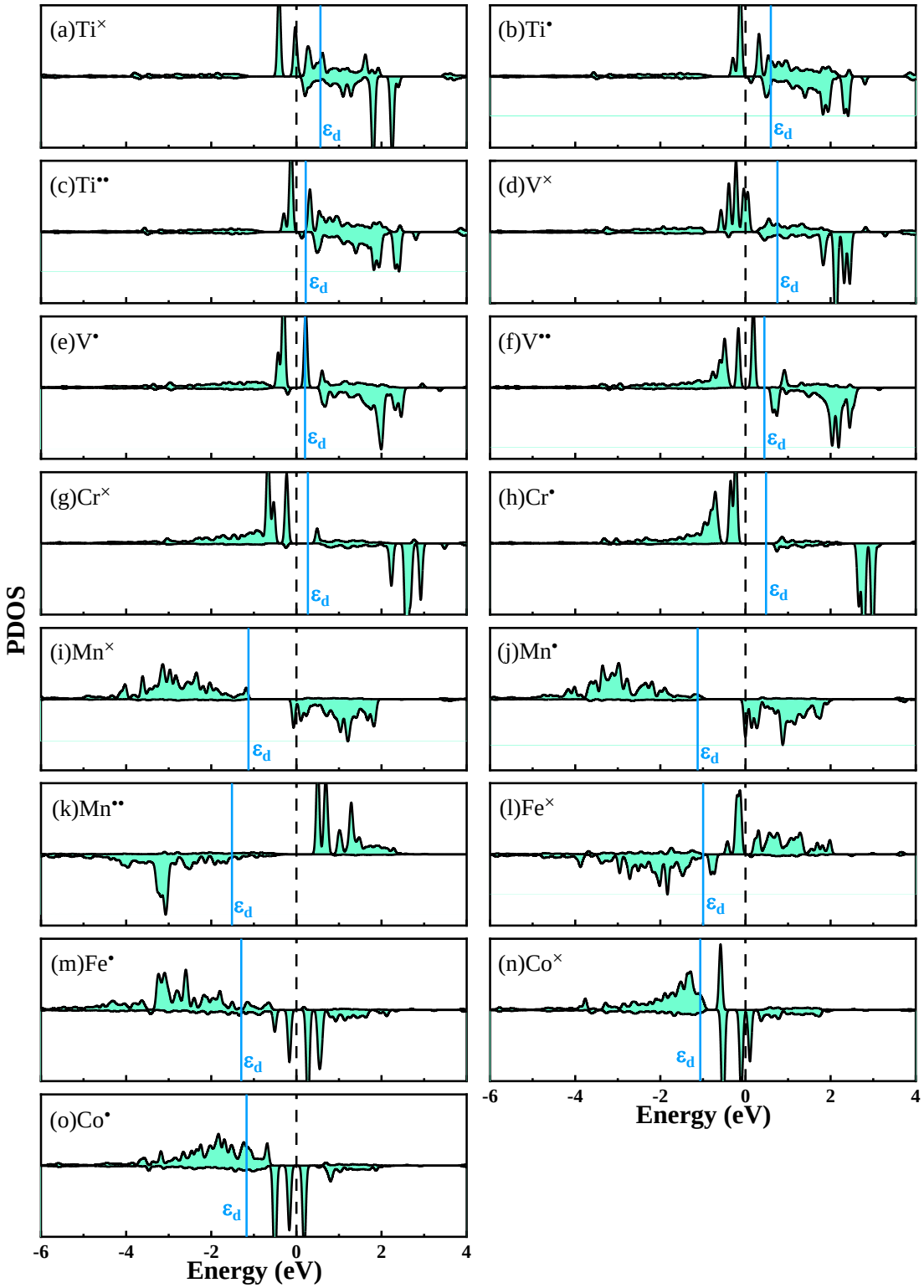

Fig. S14. (a) to (o) depict the partial density state of d-orbitals for Ti, V, Cr, Mn, Fe, and Co atoms in TM@$PtSe_2$, ε_d is the averaged-band center, the Fermi level is set to zero.

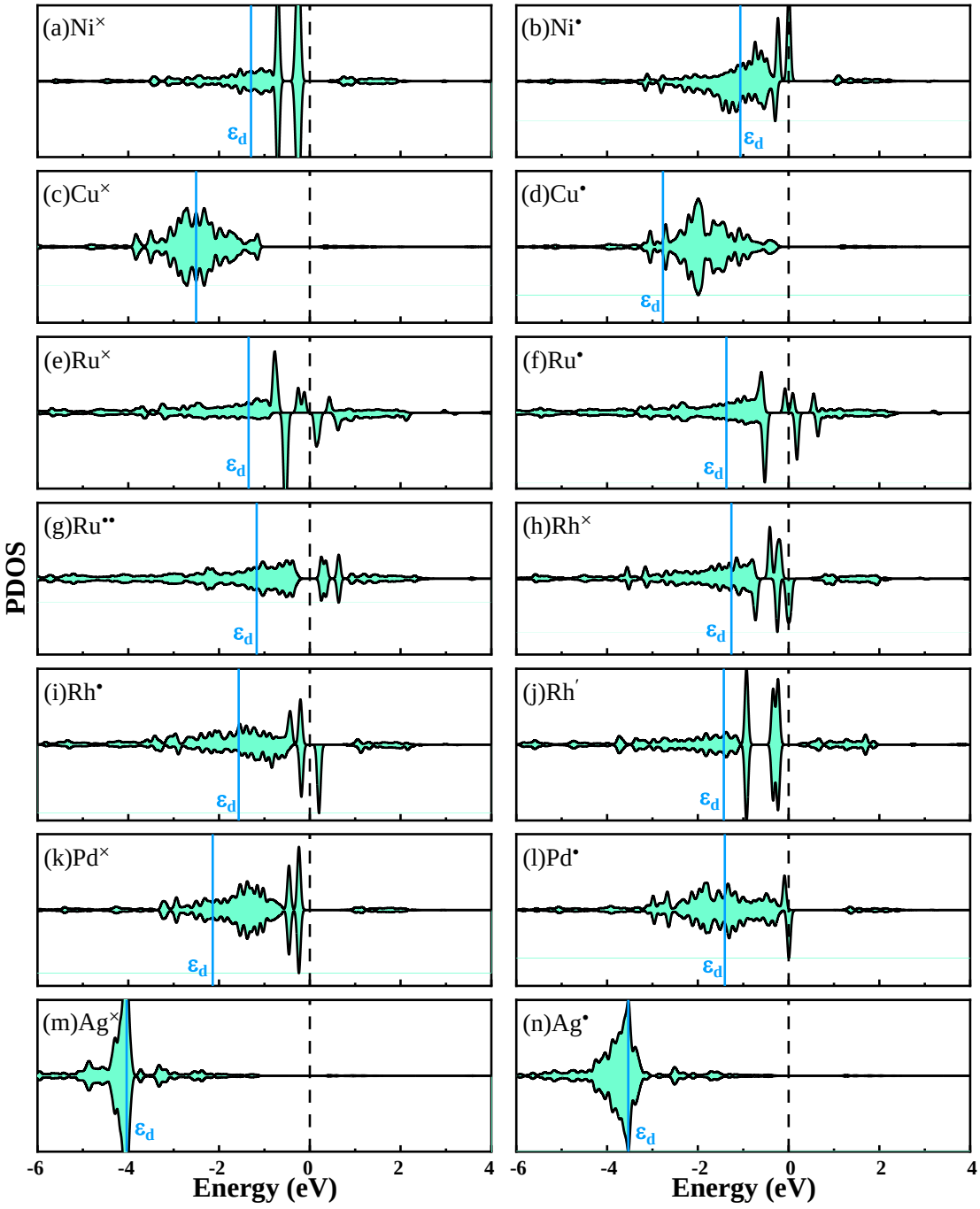

Fig. S15. (a) to (n) depict the partial density state of d-orbitals for Ni, Cu, Ru, Rh, Pd, Ag atom in TM@$PtSe_2$, ε_d is the averaged-band center, the Fermi level is set to zero.

As can be seen from **Figs. S14** and **S15**, the values of εd for TM@$PtSe_2$, except for V, Fe, and Rh, TM atoms move toward the negative energy region with the increase of atomic number. The different amounts of ε_d shifted from the Fermi energy means different adsorption strengths of the intermediates. This result shows the different interactions of the TM-d orbital with the electronic states of adsorbates, leading to the formation of bonding and antibonding states (**Figs. S18** and **S19**). Usually, a lower ε_d leads to a higher occupancy of antibonding states, thus weakening the adsorption and

vice versa. Yamada's work[38] also reported a good description of the d-band center of TM atoms on the catalytic nature. Taking the Pd•@$PtSe_2$ (-2.140) and Pd×@$PtSe_2$ (-1.405) as examples, it is observed that not a very low or high d-band center enables the two SACs to exhibit proper adsorption energy resulting in an ideal electrocatalytic property. The detailed data for each system is summarized in **Table S13.**

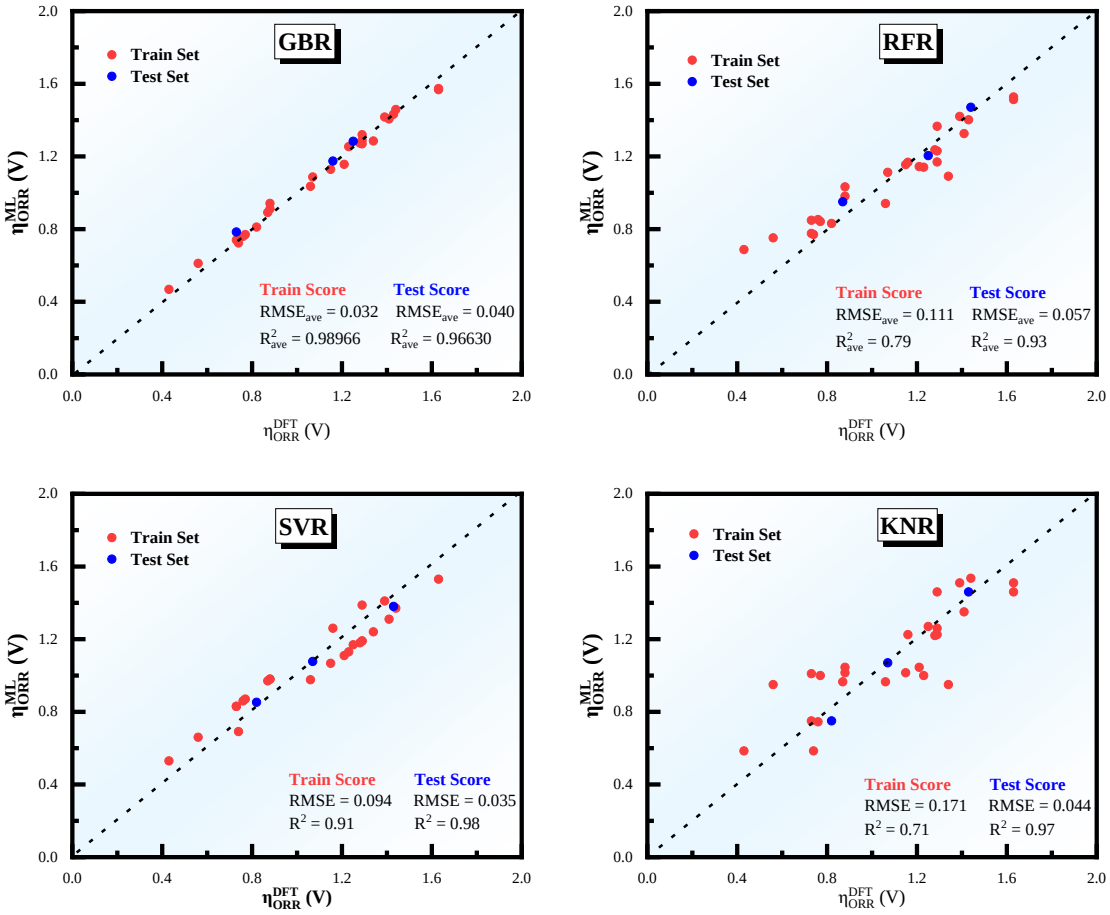

Fig. S16. A comparison of the DFT and GBR/ RFR/ SVR/KNR algorithms predicted overpotential for ORR.

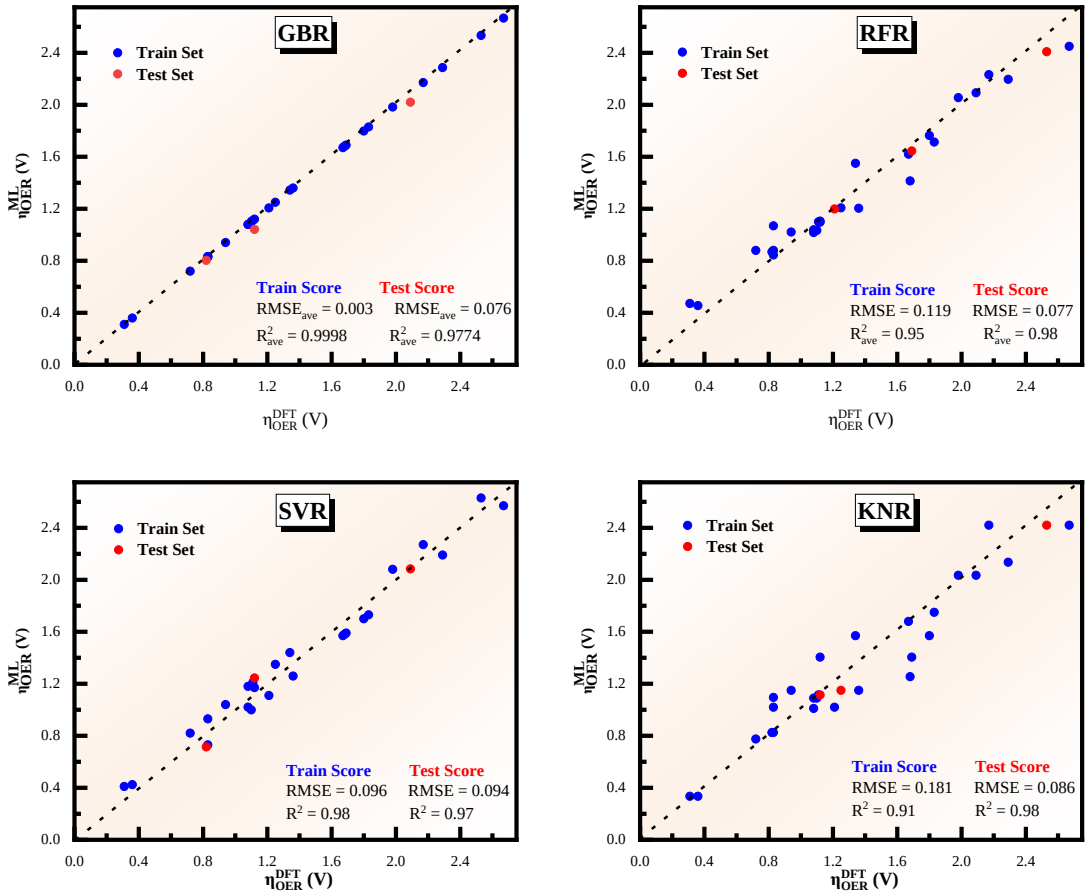

Fig. S17. A comparison of the DFT and GBR/ RFR/ SVR/ KNR algorithms predicted overpotential for OER.

Figs. S16 and **S17** show the RMSE and R^2 for the different algorithmic models of ORR and OER, respectively. The GBR algorithm has the best-fit results, thus predicting the RMSE is 0.032 V and the R^2 is 0.990 for the ORR training set. The RMSE is 0.040 V in the test set, and the R^2 is 0.966. The predicted RMSE of the OER training set is 0.003 V, while the R^2 is 0.999. The RMSE is 0.076 V in the test set, and the R^2 is 0.977. The RFR algorithm also has better fitting results, but the prediction accuracy is lower than that of the GBR algorithm. The SVR and KNR algorithms have higher RMSE and lower R^2 in both the test set and training set, thus indicating that the prediction results of these two algorithms are inaccurate. The results show that the GBR algorithm is reliable in predicting the catalytic activity after training; thus, the GBR algorithm is selected further to predict the catalytic performance of ORR and OER.

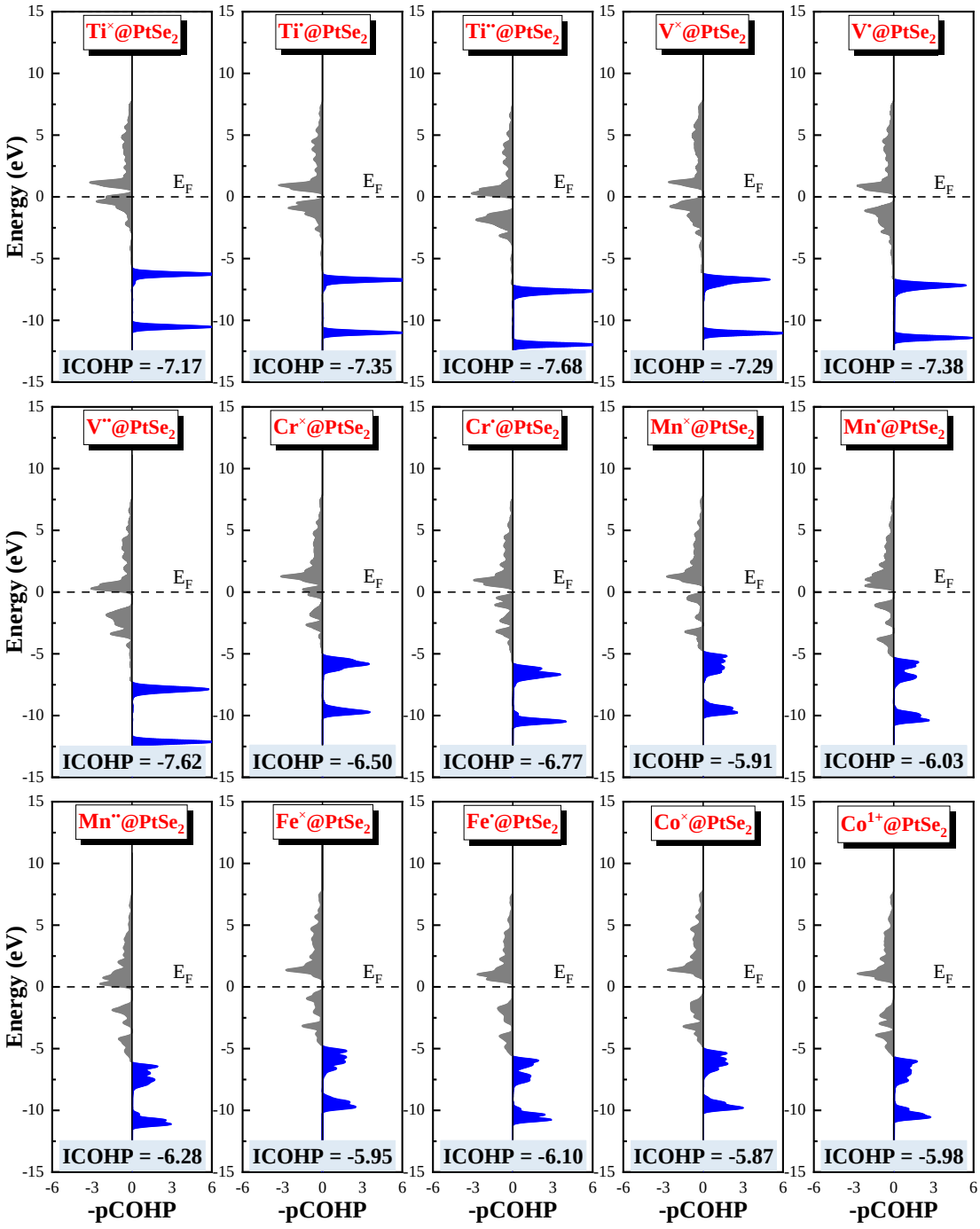

Fig. S18. The projected crystal orbital Hamilton population (pCOHP) of TM@$PtSe_2$ systems which is between TM (TM= Ti, V, Cr, Mn, Fe, and Co) d-band center and OH intermediate. E_F denotes the Fermi level. The bonding and antibonding contributions are displayed on the right and left.

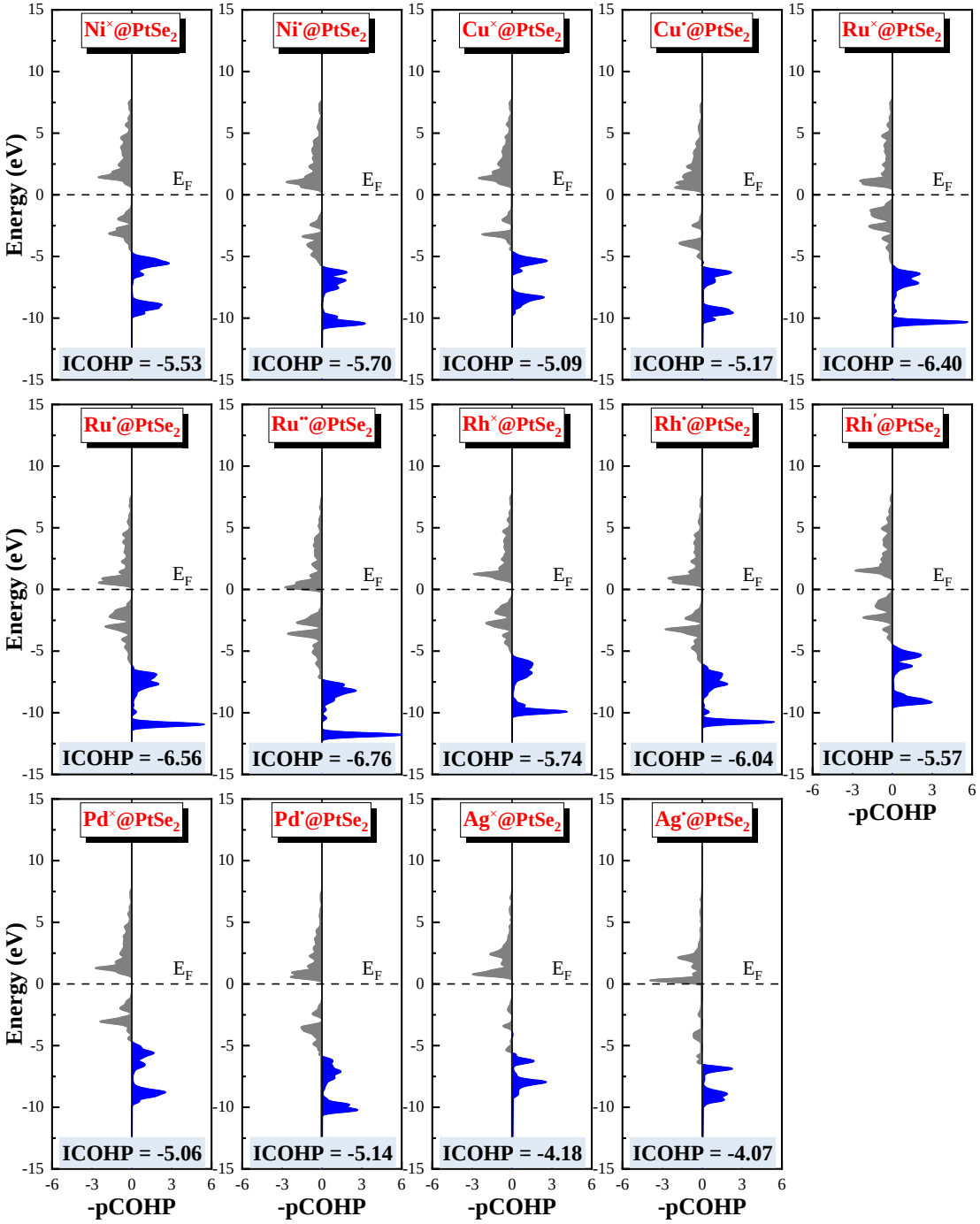

Fig. S19. The projected crystal orbital Hamilton population (pCOHP) of TM@$PtSe_2$ systems which is between TM (TM= Ni, Cu, Ru, Rh, Pd and Ag) d-band center and OH intermediate. E_F denotes the Fermi level. The bonding and antibonding contributions are displayed on the right and left.To further understand the nature of the adsorption behavior of oxygenated intermediates and display the bonding interaction relationship between TM and oxygenated intermediates more intuitively, we introduce the projected COHP(pCOHP) and the integrated value of COHP (ICOHP) to analyze the bonding and antibonding states after the *OH intermediate is adsorbed on metal pairs. Herein, the pCOHP is plotted to draw

the bonding contributions to the right and the antibonding contributions to the left. The more negative ICOHP values are the stronger the bonding interaction of TM− OH is, based on previous research[39]. Thus, the bond interactions between *OH intermediate and $PtSe_2$ systems weaken after increasing d electrons. Meanwhile, the charged systems display reduced ICOHPs compared to their neutral counterparts, meaning that the accession of charge states can enhance the mutual relationship between the TM atoms and *OH intermediate. This result implies that the charge state potentially boosts electron occupancy in the TM-O bond's bonding states, thereby reinforcing the TM-O bond.

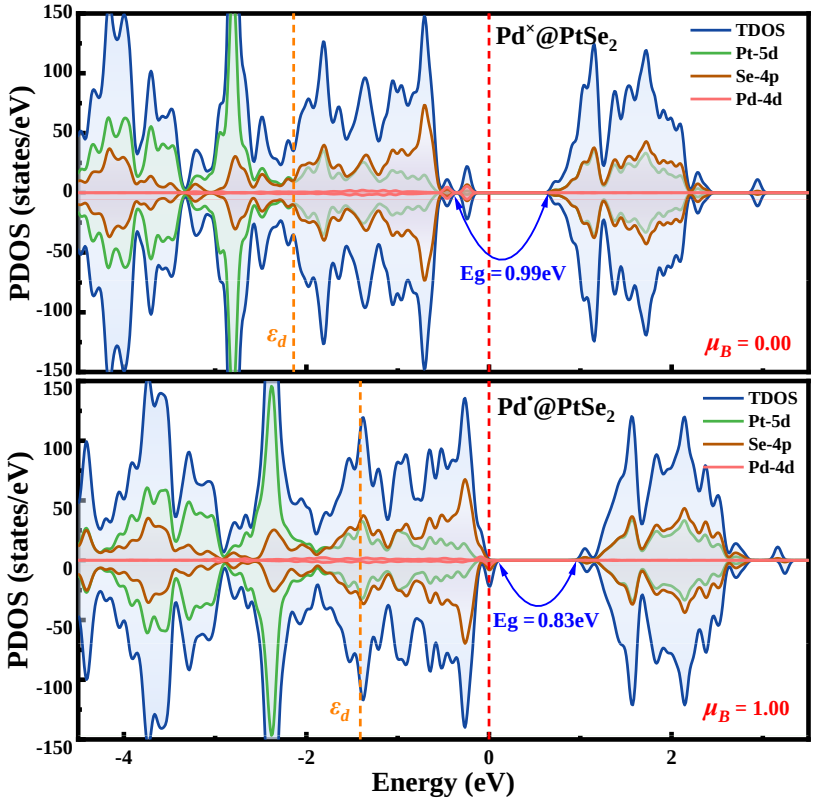

Fig. S20 The density of states (DOS) and partial density of states (PDOS) for $Pd^{\bullet}@PtSe_2$ and $Pd^{\times}@PtSe_2$ systems are calculated by the PBE method, where the Fermi level is set to zero.

The band gap of the charged system $Pd^{\bullet}@PtSe_2$ (0.83eV) is lower than that of the neutral system $Pd^{\times}@PtSe_2$ (0.99eV), and $Pd^{\bullet}@PtSe_2$ have a moderate spin moment(μ_B = 1.00), which proves advantageous for both OER and ORR.

Table S1. Experimental lattice constants of impurity-related phases (Ti, V, Cr, Mn, Fe, Co, Ni, Cu, Ru, Rh, Pd, and Ag) are used for the PBE functional calculations. The values a, b, and c are in Å.

	Space group	Experiment
TiSe	$P6_3/mmc$	a=b=3.566, c=6.233; α=β=90°, γ= 120°[40]
$TiSe_2$	$P\bar{3}m1$	a=b=3.535, c=6.011; α=β=90°, γ= 120°[41]
VSe	$P6_3/mmc$	a=b=3.918, c=5.528; α=β=90°, γ= 120°[42]
VSe_2	$P\bar{3}m1$	a=b=3.356, c=6.150; α=β=90°, γ= 120°[43]
V_3Se_4	C2/m	a=13.247, b=3.463, c=6.204; α=90°, β=116.190°, γ =90°[44]
CrSe	$P6_3/mmc$	a=b=3.680, c=6.060; α=β=90°, γ= 120°[45]
$CrSe_2$	$P\bar{3}m1$	a=b=3.399, c=5.915; α=β=90°, γ= 120°[46]
Cr_2Se_3	$R\bar{3}$	a=b=6.254, c=17.382; α=β=90°, γ= 120°[47]
MnSe	$P6_3/mmc$	a=b=3.630, c=5.910; α=β=90°, γ= 120°[48]
$MnSe_2$	$Pa\bar{3}$	a=b=c=6.417; α=β=γ=90°[49]
FeSe	P4/mmm	a=b=2.960, c=4.730; α=β=γ=90°[50]
$FeSe_2$	Pnnm	a=4.800, b=5.782, c=3.583; α=β=γ=90°[51]
Fe_3Se_4	C2/m	a=12.704, b=3.541, c=6.208; α=90°, β=117.431°, γ =90°[52]
CoSe	$P6_3/mmc$	a=b=3.620, c=5.286; α=β=90°, γ= 120°[53]
$CoSe_2$	Pnnm	a=4.840, b=5.720, c=3.600; α=β=γ=90°[54]
Co_3Se_4	C2/m	a=11.931, b=3.573, c=6.136; α=90°, β=119.325°, γ =90°[55]
NiSe	$P6_3/mmc$	a=b=4.040, c=6.710; α=β=90°, γ= 120°[56]
$NiSe_2$	$Pa\bar{3}$	a=b=c=5.965; α=β=γ=90°[57]
Ni_3Se_2	R32	a=b=6.034, c=7.251; α=β=90°, γ= 120°[58]
CuSe	$P6_3/mmc$	a=b=3.691, c=11.442; α=β=90°, γ= 120°[59]
$CuSe_2$	$Pa\bar{3}$	a=b=c=6.119; α=β=γ=90°[59]
Cu_3Se_2	$P\bar{4}2_1m$	a=b=6.406, c=4.279; α=β=γ=90°[60]
$RuSe_2$	$Pa\bar{3}$	a=b=c=5.932; α=β=γ=90°[61]
RhSe	$P6_3/mmc$	a=b=3.650, c=5.530; α=β=90°, γ= 120°[45]
$RhSe_2$	$Pa\bar{3}$	a=b=c=6.012; α=β=γ=90°[62]
PdSe	$P4_2/m$	a=b=6.730, c=6.910; α=β=γ=90°[63]
$PdSe_2$	Pbca	a=5.741, b=5.866, c=7.691; α=β=γ=90°[64]
AgSe	$F\bar{4}3m$	a=b=c=5.650; α=β=γ=90°[65]
Ag_2Se	$P2_12_12_1$	a=4.337, b= 7.070, c= 7.773; α=β=γ=90°[66]

Table S2. Calculated formation enthalpy per formula unit of impurity-related phases in TM@$PtSe_2$ by PBE functional calculation. Oqmd[17, 67] values (the Open Quantum Materials Database will be freely available for public use at https://oqmd.org/) are provided for comparison. (unit:eV)

	PBE	Oqmd
$\triangle H_f(TiSe)$	-2.26	-2.33
$\triangle H_f(TiSe_2)$	-3.41	-3.36
$\triangle H_f(VSe)$	-1.05	-1.26
$\triangle H_f(VSe_2)$	-2.43	-2.10
$\triangle H_f(V_3Se_4)$	-5.63	-5.05
$\triangle H_f(CrSe)$	0.05	-0.88
$\triangle H_f(CrSe_2)$	-1.09	-1.45
$\triangle H_f(Cr_2Se_3)$	-1.22	-2.68
$\triangle H_f(MnSe)$	-0.10	-0.76
$\triangle H_f(MnSe_2)$	-0.70	-1.41
$\triangle H_f(FeSe)$	0.59	-0.56
$\triangle H_f(FeSe_2)$	-1.27	-1.08
$\triangle H_f(Fe_3Se_4)$	-2.04	-2.21
$\triangle H_f(CoSe)$	-0.49	-0.57
$\triangle H_f(CoSe_2)$	-1.13	-0.95
$\triangle H_f(Co_3Se_4)$	-2.52	-2.09
$\triangle H_f(NiSe)$	-0.59	-0.60
$\triangle H_f(NiSe_2)$	-0.84	-0.82
$\triangle H_f(Ni_3Se_2)$	-1.64	-1.41
$\triangle H_f(RuSe_2)$	-1.40	-1.28
$\triangle H_f(RhSe)$	-0.47	-0.70
$\triangle H_f(RhSe_2)$	-1.24	-1.33
$\triangle H_f(PdSe)$	-0.69	-0.66
$\triangle H_f(PdSe_2)$	-0.92	-0.85
$\triangle H_f(AgSe)$	0.12	-0.14
$\triangle H_f(AgSe_2)$	-0.26	-0.25

Table S3. The PBE functional calculated chemical potentials at the representative chemical potential limits imposed by the formation of competing for impurity-related phases for transition metal single atoms. All energies are given in eV.

Chemical potentials	Pt rich	Se rich
μ_{Pt}	-6.08	-7.33
μ_{Se}	-4.10	-3.47
μ_{Ti}	-9.87	-11.12
μ_{V}	-9.87	-11.12
μ_{Cr}	-9.30	-10.55
μ_{Mn}	-8.90	-9.60
μ_{Fe}	-8.10	-9.35
μ_{Co}	-6.84	-7.96
μ_{Ni}	-5.52	-6.23
μ_{Cu}	-3.73	-4.03
μ_{Zr}	-11.40	-12.88
μ_{Nb}	-11.62	-13.03
μ_{Mo}	-11.78	-13.03
μ_{Ru}	-9.28	-10.53
μ_{Rh}	-7.28	-8.52
μ_{Pd}	-5.27	-6.13
μ_{Ag}	-2.71	-2.84
μ_{Hf}	-12.81	-14.11
μ_{Ta}	-13.10	-14.56
μ_{W}	-13.47	-14.72
μ_{Re}	-12.41	-13.66
μ_{Os}	-11.10	-11.82
μ_{Ir}	-8.84	-9.97

Table S4. The zero-point energy (ZPE) and entropy (S) of adsorption species and the gas molecular of water and hydrogen from the DFT calculation at 298.15 K (T).

Adsorption species	ZPE (eV)	TS (eV)
*OH	0.35	0.0
*O	0.06	0.1
*OOH	0.46	0.0
H_2O	0.56	0.58
H_2	0.27	0.40

Table S5. The Gibbs free energy (G) of gas $O_2(g)$, $H_2(g)$ and liquid water H_2O (l) at 1/0.035 bar and 298.15 K, E presents the free energy calculated from DFT, and ΔE is the Frequency correction energy.

Molecular	Pressure/bar	Temperature/K	E(DFT)/eV	ΔE/eV	G/eV
$O_2(g)$	1	298.15	--	--	-9.91
$H_2(g)$	1	298.15	-6.76	-0.045	-6.8
$H_2O(l)$	0.035	298.15	-14.22	-0.001	-14.22

Table S6. The bond length between TM and the adjacent atoms (Se), as well as the charge transfer between TM and the neighboring atoms (Se) and the adsorbed species (*OH, *O, *OOH)

TM	Bond length(Å)			Charge transfer(e)						
	d_{TM-Se1}	d_{TM-Se2}	d_{TM-Se3}	Q_{TM}	Q_{Se1}	Q_{Se2}	Q_{Se3}	Q_{*OH}	Q_{*O}	Q_{*OOH}
Ti$^{\times}$	2.54	2.54	2.54	-1.08	0.28	0.28	0.28	0.49	0.82	0.42
Ti$^{\bullet}$	2.56	2.54	2.56	-1.15	0.27	0.36	0.27	0.47	0.76	0.52
Ti$^{\bullet\bullet}$	2.58	2.57	2.58	-1.19	0.28	0.28	0.28	0.42	0.70	0.54
V$^{\times}$	2.40	2.56	2.56	-0.98	0.34	0.21	0.22	0.45	0.68	0.41
V$^{\bullet}$	2.48	2.57	2.57	-1.05	0.33	0.24	0.24	0.44	0.67	0.41
V$^{\bullet\bullet}$	2.57	2.57	2.57	-1.03	0.27	0.26	0.26	0.41	0.62	0.43
Cr$^{\times}$	2.38	2.64	2.65	-0.83	0.18	0.17	0.18	0.53	0.61	0.44
Cr$^{\bullet}$	2.62	2.63	2.63	-0.79	0.18	0.18	0.18	0.48	0.64	0.43
Mn$^{\times}$	2.60	2.70	2.64	-0.67	0.19	0.17	0.18	0.55	0.65	0.54
Mn$^{\bullet}$	2.73	2.74	2.74	-0.73	0.18	0.18	0.18	0.53	0.58	0.67
Mn$^{\bullet\bullet}$	2.74	2.74	2.74	-0.92	0.20	0.21	0.20	0.46	0.54	0.35
Fe$^{\times}$	2.30	2.42	2.42	-0.59	0.22	0.15	0.15	0.52	0.67	0.47
Fe$^{\bullet}$	2.33	2.50	2.50	-0.69	0.24	0.15	0.15	0.49	0.63	0.50
Co$^{\times}$	2.33	2.33	2.32	-0.40	0.10	0.09	0.09	0.46	0.67	0.46
Co$^{\bullet}$	2.41	2.42	2.42	-0.49	0.14	0.15	0.15	0.44	0.60	0.41
Ni$^{\times}$	2.33	2.33	2.33	-0.28	0.09	0.09	0.09	0.48	0.59	0.38
Ni$^{\bullet}$	2.38	2.38	2.38	-0.39	0.12	0.11	0.11	0.39	0.50	0.32
Cu$^{\times}$	2.46	2.46	2.46	-0.32	0.09	0.09	0.09	0.53	0.61	0.51
Cu$^{\bullet}$	2.45	2.46	2.46	-0.42	0.12	0.12	0.12	0.46	0.49	0.28
Ru$^{\times}$	2.34	2.45	2.45	-1.25	0.06	0.04	0.04	0.39	0.63	0.40
Ru$^{\bullet}$	2.33	2.42	2.44	-1.28	0.04	0.06	0.05	0.37	0.55	0.36
Ru$^{\bullet\bullet}$	2.34	2.39	2.39	-1.30	0.05	0.06	0.06	0.32	0.47	0.31
Rh$^{\times}$	2.41	2.45	2.45	-1.10	0.03	0.03	0.01	0.39	0.59	0.35
Rh$^{\bullet}$	2.45	2.46	2.46	-1.20	0.05	0.05	0.05	0.34	0.56	0.28
Rh′	2.41	2.42	2.42	-1.01	-0.01	-0.01	-0.01	0.44	0.64	0.41
Pd$^{\times}$	2.53	2.54	2.55	-1.09	0.02	0.02	0.02	0.42	0.56	0.33
Pd$^{\bullet}$	2.53	2.54	2.55	-1.16	0.03	0.03	0.03	0.33	0.44	0.26
Ag$^{\times}$	2.75	2.77	2.78	-1.24	0.05	0.05	0.06	0.53	0.54	0.49
Ag$^{\bullet}$	2.74	2.75	2.77	-1.37	0.08	0.09	0.08	0.41	0.41	0.18

Apart from V$^{\times}$, Cr$^{\times}$, Fe$^{\times}$, and Fe$^{\bullet}$ @$PtSe_2$ systems, the TM-Se1, TM-Se2, and TM-Se3 bonds of other TM@$PtSe_2$ systems are approximately equal in length, with the range of 2.30 - 2.78 Å. In systems with different bond lengths,

the shorter the bond length, the more charge transfer. For example, in the $Fe^{\times}$ system, the bond length between the Fe atom and Se1 is shorter, and more charges are transferred.

Table S7. The ΔG_{*OH}, ΔG_{*O}, and ΔG_{*OOH} of TM@$PtSe_2$ are calculated using the PBE (without solvation) and PBE+SOL (with solvation) methods in TM@$PtSe_2$ systems (unit: eV).

	PBE			PBE+SOL		
TM	ΔG_{*OH}	ΔG_{*O}	ΔG_{*OOH}	ΔG_{*OH}	ΔG_{*O}	ΔG_{*OOH}
Ti$^{\times}$	-1.91	-1.59	1.62	-0.21	-0.05	3.35
Ti$^{\bullet}$	-1.86	-1.45	1.64	-0.13	-0.54	3.36
Ti$^{\bullet\bullet}$	-1.68	-1.15	1.82	-0.04	-0.20	3.56
V$^{\times}$	-1.40	-1.20	1.99	-0.40	-0.27	3.24
V$^{\bullet}$	-1.36	-0.97	2.23	-0.20	0.29	3.60
V$^{\bullet\bullet}$	-1.57	-1.15	1.75	-0.06	0.22	3.43
Cr$^{\times}$	-0.57	-0.09	2.68	0.08	0.61	3.64
Cr$^{\bullet}$	-0.58	0.00	2.43	0.35	0.97	3.54
Mn$^{\times}$	-0.75	0.25	2.53	0.02	1.08	3.53
Mn$^{\bullet}$	-0.91	0.35	3.17	0.16	1.52	4.43
Mn$^{\bullet\bullet}$	-0.13	0.93	2.98	1.33	2.51	4.57
Fe$^{\times}$	-0.65	0.40	2.55	-0.18	0.83	3.31
Fe$^{\bullet}$	-0.66	0.57	2.60	-0.05	1.16	3.47
Co$^{\times}$	-0.40	0.51	2.72	-0.06	0.72	3.32
Co$^{\bullet}$	-0.32	0.93	2.79	0.07	1.34	3.51
Ni$^{\times}$	0.31	1.68	3.35	0.51	1.75	3.81
Ni$^{\bullet}$	0.19	1.50	3.16	0.47	1.77	3.72
Cu$^{\times}$	0.08	2.22	3.30	0.17	2.24	3.70
Cu$^{\bullet}$	0.98	2.95	3.96	1.23	3.29	4.56
Ru$^{\times}$	-0.30	-0.11	2.51	0.00	0.20	3.13
Ru$^{\bullet}$	-0.41	-0.26	2.42	-0.06	0.16	3.06
Ru$^{\bullet\bullet}$	-0.39	-0.38	2.49	-0.01	0.09	3.18
Rh$^{\times}$	-0.18	1.09	3.15	0.41	1.25	3.59
Rh$^{\bullet}$	0.20	0.95	3.10	0.46	1.27	3.62
Rh′	0.27	1.34	3.38	0.50	1.46	3.81
Pd$^{\times}$	1.16	2.87	4.03	1.28	2.88	4.43
Pd$^{\bullet}$	0.68	2.46	3.76	1.16	2.70	4.12
Ag$^{\times}$	0.57	2.97	3.78	0.67	2.99	4.19
Ag$^{\bullet}$	1.64	3.87	4.34	1.91	4.24	5.03

The solvation effect is considered by the VASPsol code with a dielectric constant of 78.4 to simulate the H_2O solvent environment (PBE+SOL).[68] There is a difference between PBE and PBE+SOL. We have used the results obtained with PBE+SOL for our subsequent analysis.

Table S8. The optimized structures of *OH, *O and *OOH intermediates on the different TM@$PtSe_2$ systems.

	*OH		*O		*OOH	
TM	Top view	side view	Top view	side view	Top view	side view
$Ti^{\times}$	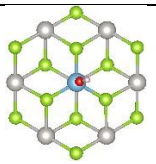	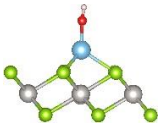	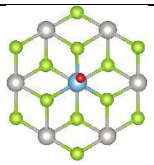	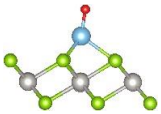	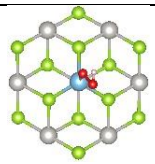	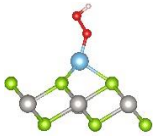
$Ti^{\bullet}$	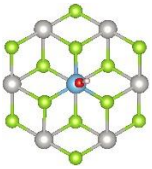	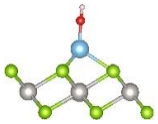	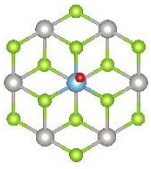	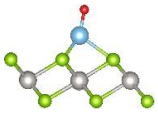	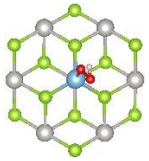	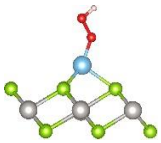
$Ti^{\bullet\bullet}$	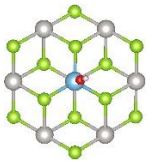	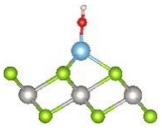	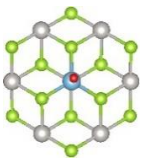		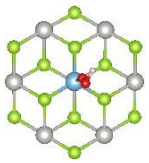	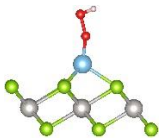
$V^{\times}$	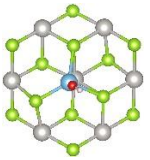	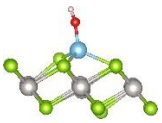	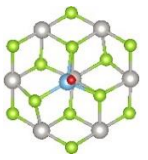	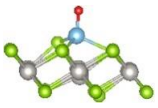	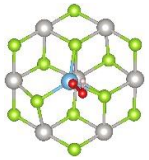	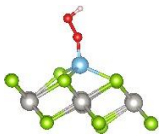
$V^{\bullet}$	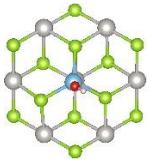	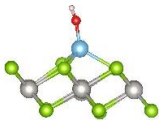	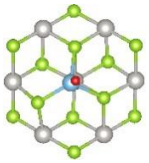		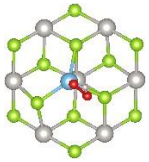	
$V^{\bullet\bullet}$	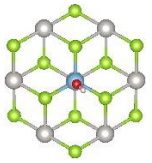		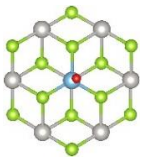	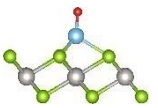	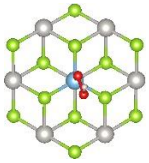	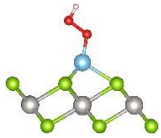
$Cr^{\times}$	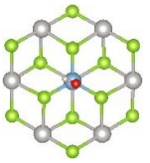	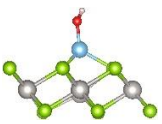	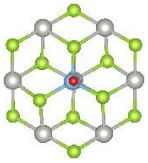		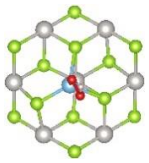	
$Cr^{\bullet}$	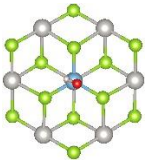		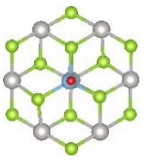	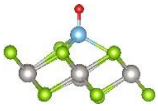	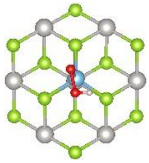	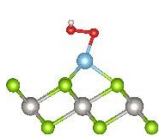
$Mn^{\times}$	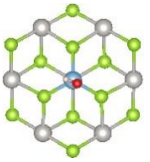		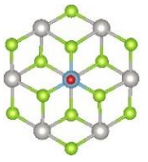		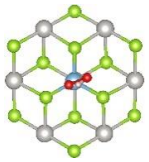	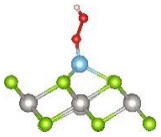

Pt Se O H TM (Ti、V、Cr、Mn)

	*OH		*O		*OOH	
TM	Top view	side view	Top view	side view	Top view	side view
$Mn^{\bullet}$	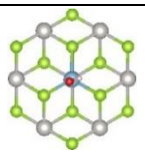		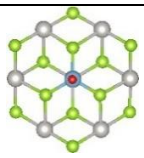		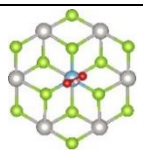	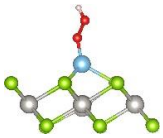
$Mn^{\bullet\bullet}$	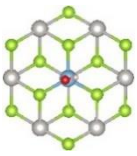	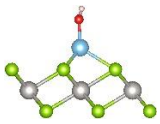	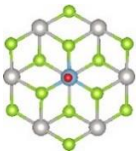		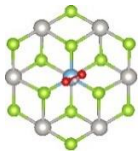	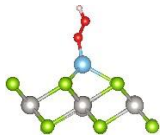
$Fe^{\times}$	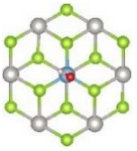	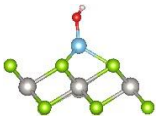	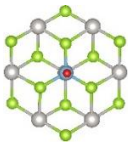			
$Fe^{\bullet}$	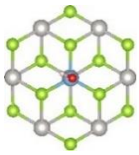	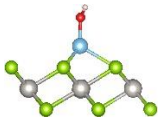	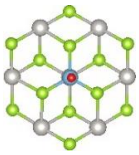			
$Co^{\times}$	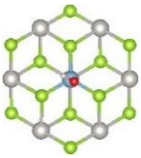	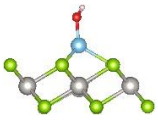	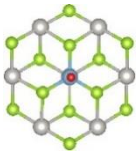		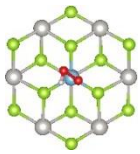	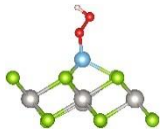
$Co^{\bullet}$	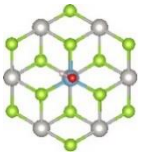	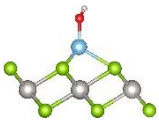	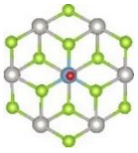	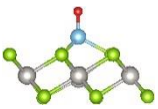	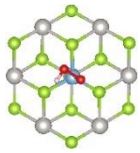	
$Ni^{\times}$	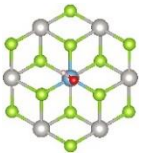	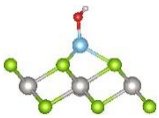	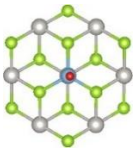	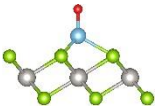		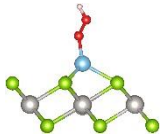
$Ni^{\bullet}$	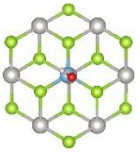				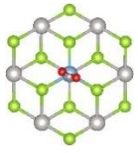	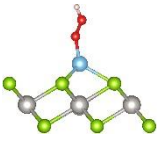
$Cu^{\times}$	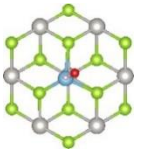		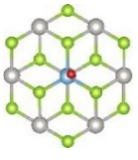	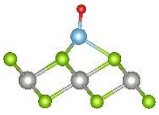		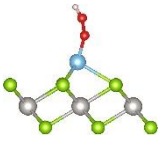
$Cu^{\bullet}$	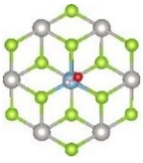	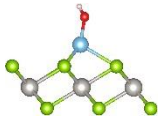	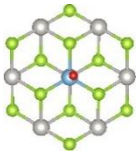	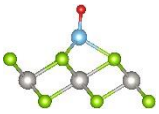	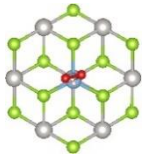	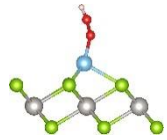

Pt Se O H TM (Mn、Fe、Co、Ni、Cu)

	*OH		*O		*OOH	
TM	Top view	side view	Top view	side view	Top view	side view
Ru×	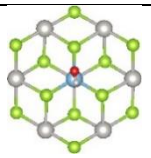	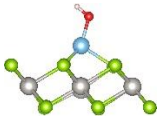	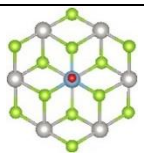	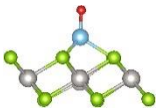		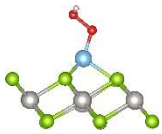
Ru•	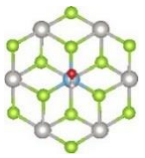	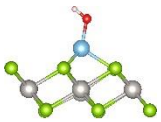	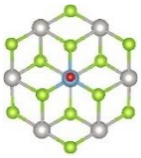	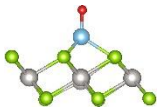	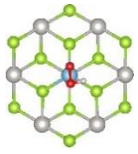	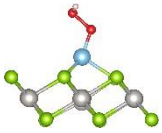
Ru••	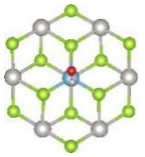	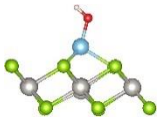	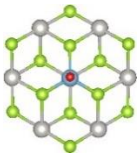		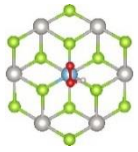	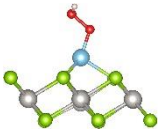
Rh×		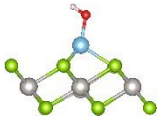	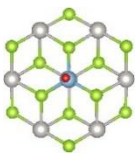	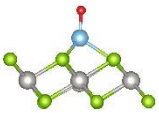	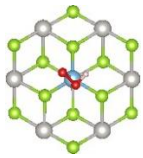	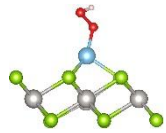
Rh•	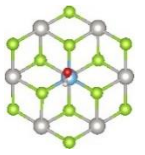	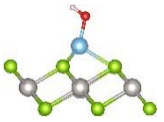	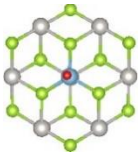			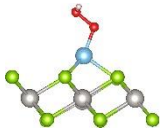
Rh′	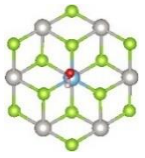	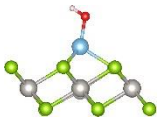	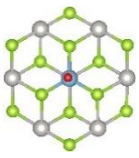	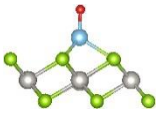		
Pd×	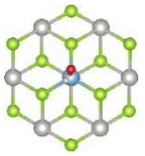	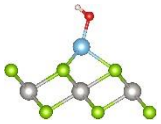	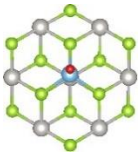	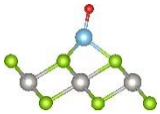	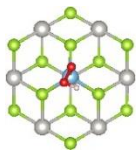	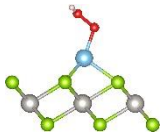
Pd•	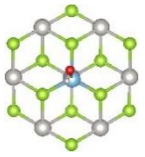	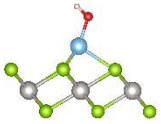	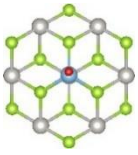	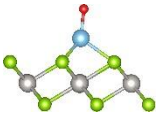		
Ag×			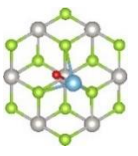	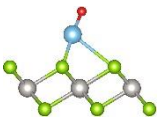	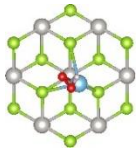	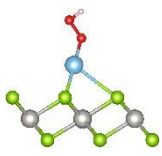
Ag•	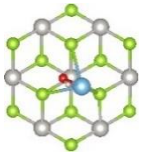	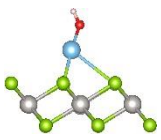	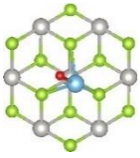	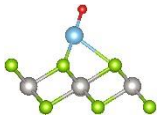	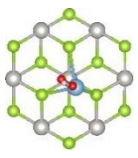	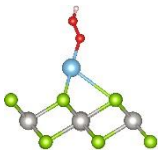

Pt Se O H TM (Ru、Rh、Pd、Ag)

The structures of *O and *OH are not significantly different among the various systems, while there is a large difference in *OOH structures. This means that the defect charge can significantly affect the structure of *OOH, thereby influencing the adsorption strength.

Table S9. The Gibbs free energy change between two intermediate processes, slab to *OH (ΔG_1), *OH to *O (ΔG_2), *O to *OOH (ΔG_3) and *OOH to O_2 (ΔG_4) (unit: eV) of TM@$PtSe_2$ system(the system of anchoring other transition metal atoms that we did not discuss in the main text), as well as the corresponding OER overpotential (η^{OER}) and ORR overpotential (η^{ORR}) (unit: eV) (unit: eV) are calculated by PBE (without solvation) and PBE+SOL (with solvation) methods in TM@$PtSe_2$ systems. .

	PBE						PBE+SOL					
TM	ΔG_1	ΔG_2	ΔG_3	ΔG_4	η^{OER}	η^{ORR}	ΔG_1	ΔG_2	ΔG_3	ΔG_4	η^{OER}	η^{ORR}
$Zr^{\times}$	-2.5	0.3	3.29	3.48	2.25	3.38	-4.15	2.62	3.62	2.83	2.39	5.38
$Zr^{\bullet}$	-2.26	-1.93	1.35	4.92	2.34	3.49	-1.94	0.34	3.6	2.92	2.37	1.94
$Zr^{\bullet\bullet}$	-2.04	0.29	3.25	3.42	2.19	3.27	-1.72	0.29	3.58	2.77	2.35	2.95
$Nb^{\times}$	-1.85	-0.07	3.53	3.31	2.08	3.08	-1.53	-0.07	3.86	2.66	2.63	2.76
$Nb^{\bullet}$	-1.68	-0.10	3.47	3.23	2.24	2.91	-1.36	-0.10	3.80	2.58	2.57	2.59
$Nb^{\bullet\bullet\bullet}$	-0.21	0.19	3.53	1.41	2.30	1.44	0.11	0.19	3.86	0.76	2.63	1.12
$Hf^{\bullet\bullet}$	0.07	0.70	2.97	1.18	1.74	1.16	-1.05	2.93	1.91	1.13	1.70	2.28
Hf'	0.84	0.52	3.03	0.53	1.80	0.71	0.97	0.38	3.46	0.11	2.23	1.12
$Ta^{\bullet\bullet}$	0.25	-0.17	3.73	1.01	2.50	0.88	0.34	0.38	3.47	0.73	2.24	0.89
Ta''	0.35	-0.17	3.73	1.01	2.50	0.88	0.49	-0.22	4.02	0.63	2.79	1.45
$W^{\times}$	0.32	-0.42	3.44	1.58	2.21	1.65	0.43	-0.25	3.57	1.17	2.34	1.48
$W^{\bullet}$	0.35	-0.10	3.33	1.34	2.10	1.33	0.52	0.04	3.55	0.81	2.32	1.19
$W^{\bullet\bullet}$	0.56	-0.17	3.31	1.22	2.08	1.40	0.78	-0.06	3.55	0.81	2.32	1.19
$Os^{\times}$	-0.70	-0.30	3.13	2.79	1.90	1.93	-0.52	-0.22	3.42	2.24	2.19	1.75
$Os^{\bullet}$	-0.84	-0.10	3.05	2.81	1.82	2.07	-0.59	-0.02	3.34	2.19	2.11	1.82
$Os^{\bullet\bullet}$	-0.59	-0.44	3.51	2.44	2.28	1.82	-0.38	-0.29	3.76	1.83	2.53	1.61
$Ir^{\times}$	-0.27	0.76	2.29	2.14	1.06	1.50	-0.08	0.69	2.64	1.67	1.41	1.31
$Ir^{\bullet}$	-0.18	0.56	2.53	2.01	1.30	1.41	0.03	0.61	2.80	1.48	1.57	1.20
Ir'	-0.05	0.60	2.39	1.98	1.16	1.28	0.15	0.58	2.66	1.53	1.43	1.08

Table S10. The Gibbs free energy change between two intermediate processes, slab to *OH (ΔG_1), *OH to *O (ΔG_2), *O to *OOH (ΔG_3) and *OOH to O_2 (ΔG_4) (unit: eV) of TM@$PtSe_2$ system, as well as the corresponding OER overpotential (η^{OER}) and ORR overpotential (η^{ORR}) (unit: eV) are calculated by PBE (without solvation) and PBE+SOL (with solvation) methods in TM@$PtSe_2$ systems.

	PBE						PBE+SOL					
TM	ΔG_1	ΔG_2	ΔG_3	ΔG_4	η^{OER}	η^{ORR}	ΔG_1	ΔG_2	ΔG_3	ΔG_4	η^{OER}	η^{ORR}
Ti$^{\times}$	-1.91	0.32	3.20	3.31	2.08	3.14	-0.21	0.16	3.40	1.57	2.17	1.44
Ti$^{\bullet}$	-1.86	0.41	3.10	3.27	2.04	3.09	-0.13	-0.40	3.90	1.55	2.67	1.63
Ti$^{\bullet\bullet}$	-1.68	0.53	2.97	3.10	1.87	2.91	-0.04	-0.16	3.76	1.36	2.53	1.39
V$^{\times}$	-1.40	0.20	3.19	2.93	1.96	2.63	-0.40	0.12	3.52	1.68	2.29	1.63
V$^{\bullet}$	-1.36	0.40	3.20	2.68	1.97	2.59	-0.20	0.49	3.32	1.31	2.09	1.43
V$^{\bullet\bullet}$	-1.57	0.41	2.91	3.17	1.94	2.80	-0.06	0.28	3.21	1.49	1.98	1.29
Cr$^{\times}$	-0.57	0.48	2.77	2.24	1.54	1.8	0.08	0.53	3.03	1.28	1.80	1.15
Cr$^{\bullet}$	-0.58	0.58	2.43	2.49	1.26	1.81	0.35	0.62	2.57	1.38	1.34	0.88
Mn$^{\times}$	-0.75	1.00	2.28	2.39	1.16	1.98	0.02	1.07	2.44	1.39	1.21	1.21
Mn$^{\bullet}$	-0.91	1.26	2.82	1.75	1.59	2.14	0.16	1.36	2.91	0.49	1.68	1.07
Mn$^{\bullet\bullet}$	-0.13	1.06	2.05	1.94	0.82	1.36	1.33	1.18	2.06	0.35	0.83	0.88
Fe$^{\times}$	-0.65	1.05	2.15	2.37	1.14	1.88	-0.18	1.00	2.48	1.62	1.25	1.41
Fe$^{\bullet}$	-0.66	1.23	2.03	2.32	1.09	1.89	-0.05	1.21	2.31	1.45	1.08	1.28
Co$^{\times}$	-0.40	0.90	2.21	2.20	0.98	1.63	-0.06	0.78	2.59	1.60	1.36	1.29
Co$^{\bullet}$	-0.32	1.25	1.86	2.13	0.90	1.55	0.07	1.28	2.17	1.40	0.94	1.16
Ni$^{\times}$	0.31	1.37	1.66	1.58	0.43	0.92	0.50	1.25	2.06	1.11	0.83	0.73
Ni$^{\bullet}$	0.19	1.32	1.66	1.75	0.52	1.04	0.47	1.30	1.95	1.20	0.72	0.76
Cu$^{\times}$	0.08	2.14	1.08	1.62	0.91	1.15	0.17	2.06	1.47	1.21	0.83	1.06
Cu$^{\bullet}$	0.98	1.97	1.01	0.96	0.74	0.27	1.24	2.05	1.27	0.36	0.82	0.87
Ru$^{\times}$	-0.30	0.19	2.62	2.41	1.39	1.53	0.0	0.21	2.92	1.79	1.69	1.23
Ru$^{\bullet}$	-0.41	0.15	2.68	2.50	1.45	1.64	-0.06	0.22	2.90	1.86	1.67	1.29
Ru$^{\bullet\bullet}$	-0.39	0.01	2.87	2.43	1.64	1.62	-0.02	0.10	3.06	1.78	1.83	1.25
Rh$^{\times}$	0.18	0.91	2.06	1.77	0.83	1.05	0.41	0.84	2.34	1.33	1.11	0.82
Rh$^{\bullet}$	0.20	0.75	2.14	1.83	0.91	1.03	0.46	0.81	2.35	1.30	1.12	0.77
Rh′	0.27	1.07	2.04	1.54	0.81	0.96	0.50	0.96	2.35	1.11	1.12	0.73
Pd$^{\times}$	1.16	1.72	1.15	0.89	0.49	0.34	1.29	1.59	1.55	0.49	0.36	0.74
Pd$^{\bullet}$	0.68	1.78	1.30	1.16	0.55	0.55	1.16	1.54	1.42	0.80	0.31	0.43
Ag$^{\times}$	0.58	2.39	0.81	1.14	1.16	0.65	0.67	2.31	1.21	0.73	1.08	0.56
Ag$^{\bullet}$	1.64	2.23	0.47	0.58	1.00	0.76	1.91	2.33	0.79	-0.11	1.10	1.34

According to **Eq. S11** in **Note S3**, we can calculate the Gibbs free energy change for each step of the four-electron process. Then, using **Eqs. S14** and **S15**, we can obtain the

overpotential for OER and ORR respectively. **Table S9** refers to several groups with poor results that were not shown in the main text, while **Table S10** represents the 29 groups discussed in the main text.

Table S11. The summary of bifunctional catalysts [a]

	Catalyst	η^{OER}	η^{ORR}	ΔE
This work	Pd^{x}@$PtSe_2$	0.31 V	0.43 V	0.74 V
	Pd^{*}@$PtSe_2$	0.36 V	0.74 V	1.10 V
Other reports	Ru/C	0.39 V	0.62 V	1.01 V[69]
	MoC_2	0.45 V	0.47 V	0.92 V[70]
	$Co_3(HITP)_2$	0.36 V	0.73 V	1.09 V[71]
	Fe-based COF	0.38 V	0.48 V	0.86 V[72]
	Ni@S-GPY	0.43 V	0.36 V	0.79 V[33]
	Pt@Sb	0.48 V	0.71 V	1.19 V[73]
	Cu@MSN	0.55 V	0.65 V	1.20 V[74]
	Co@g-C_3N_4	0.53 V	0.67 V	1.20 V[75]
	Rh/V_N-CN	0.32 V	0.43 V	0.75 V[34]
	Rh/Pd@C_2N	0.37 V	0.38 V	0.75 V[76]
	Cu@Mo_2B_2	0.31 V	0.34 V	0.65 V[77]
	Ni/Pt@N_3-BP	0.44/0.25V	0.29/0.32V	0.73/0.57V[78]
	Ni@V_{Al}−2N_P−AlP	0.26 V	0.32 V	0.58 V[33]
	Pd@1T-$MoSe_2$	0.49 V	0.32 V	0.81 V[79]
	Co-DW	0.45 V	0.46 V	0.91 V[80]
	Ni@VS_2	0.31 V	0.45 V	0.86 V[81]
	Rh@C_3N	0.35 V	0.27 V	0.62 V[82]

[a] η^{OER} and η^{ORR} represent the overpotential of the OER and ORR processes. ΔE is the sum of η^{OER} and η^{ORR}.

The results obtained in this work compare favorably with the reported results so far, demonstrating excellent catalytic performance for OER, ORR, and bifunctional applications.

Table S12. The inter-atomic charge transfer (CT) in TM, O, and H among each adsorption process, where Q_{TM}, Q_O, and Q_H are the value of charge transfer in TM, O, and H atoms after absorbing the OH, and $Q_{TM'}$, $Q_{O'}$, $Q_{H'}$ are the quantities of CT in TM and O atoms in *O process, and the $Q_{TM''}$, $Q_{O''}$, $Q_{O1''}$, $Q_{H''}$represent the number of CT in TM, O and H atoms.

TM	Q_{TM*OH}			Q_{TM*O}		Q_{TM*OOH}			
	Q_{TM}	Q_O	Q_H	$Q_{TM'}$	$Q_{O'}$	$Q_{TM''}$	$Q_{O1''}$	$Q_{O2''}$	$Q_{H''}$
$Ti^{\times}$	-0.28	1.16	-0.67	-0.36	0.82	-0.36	0.48	0.56	-0.62
$Ti^{\bullet}$	-0.24	1.15	-0.68	-0.27	0.76	-0.21	0.53	0.61	-0.62
$Ti^{\bullet\bullet}$	-0.27	1.05	-0.63	-0.33	0.70	-0.15	0.54	0.65	-0.65
$V^{\times}$	-0.32	1.11	-0.66	-0.30	0.68	-0.32	0.46	0.55	-0.60
$V^{\bullet}$	-0.21	1.08	-0.64	-0.34	0.67	-0.25	0.48	0.55	-0.62
$V^{\bullet\bullet}$	-0.30	1.07	-0.66	-0.35	0.62	-0.22	0.50	0.55	-0.62
$Cr^{\times}$	-0.24	1.12	-0.59	-0.34	0.61	-0.31	0.48	0.60	-0.64
$Cr^{\bullet}$	-0.35	1.11	-0.63	-0.45	0.64	-0.33	0.43	0.64	-0.64
$Mn^{\times}$	-0.39	1.18	-0.63	-0.30	0.65	-0.41	0.49	0.68	-0.63
$Mn^{\bullet}$	-0.40	1.14	-0.61	-0.20	0.58	-0.28	0.49	0.75	-0.57
$Mn^{\bullet\bullet}$	-0.21	1.09	-0.63	-0.10	0.54	-0.23	0.38	0.63	-0.66
$Fe^{\times}$	-0.26	1.13	-0.61	-0.26	0.67	-0.40	0.45	0.64	-0.62
$Fe^{\bullet}$	-0.29	1.11	-0.62	-0.25	0.63	-0.14	0.49	0.61	-0.60
$Co^{\times}$	-0.29	1.10	-0.64	-0.36	0.67	-0.27	0.45	0.62	-0.61
$Co^{\bullet}$	-0.29	1.04	-0.60	-0.27	0.60	-0.27	0.43	0.60	-0.62
$Ni^{\times}$	-0.33	1.08	-0.60	-0.35	0.59	-0.25	0.41	0.60	-0.63
$Ni^{\bullet}$	-0.27	1.03	-0.64	-0.30	0.50	-0.27	0.38	0.57	-0.63
$Cu^{\times}$	-0.25	1.11	-0.58	-0.27	0.61	-0.25	0.49	0.61	-0.59
$Cu^{\bullet}$	-0.24	1.07	-0.61	-0.26	0.49	-0.21	0.38	0.54	-0.64
$Ru^{\times}$	-0.31	0.99	-0.60	-0.50	0.63	-0.33	0.37	0.63	-0.60
$Ru^{\bullet}$	-0.33	0.97	-0.60	-0.45	0.55	-0.34	0.37	0.64	-0.65
$Ru^{\bullet\bullet}$	-0.33	0.96	-0.64	-0.42	0.47	-0.35	0.34	0.62	-0.65
$Rh^{\times}$	-0.32	0.97	-0.58	-0.47	0.59	-0.30	0.37	0.54	-0.56
$Rh^{\bullet}$	-0.28	0.94	-0.60	-0.45	0.56	-0.27	0.34	0.57	-0.63
Rh′	-0.37	1.01	-0.57	-0.51	0.64	-0.34	0.40	0.62	-0.61
$Pd^{\times}$	-0.27	1.01	-0.59	-0.35	0.56	-0.25	0.37	0.56	-0.60
$Pd^{\bullet}$	-0.25	0.92	-0.59	-0.35	0.44	-0.26	0.32	0.54	-0.60
$Ag^{\times}$	-0.15	1.12	-0.59	-0.18	0.54	-0.16	0.45	0.64	-0.60
$Ag^{\bullet}$	-0.06	0.98	-0.57	-0.15	0.41	-0.11	0.30	0.52	-0.64

The charge transfer situation is the same for *OH, *O and *OOH intermediates on the different TM@$PtSe_2$ system. The TM atoms lose electrons, the O atoms gain electrons, and, the H atoms lose electrons except for the *O intermediates. The range of electron

loss for the TM atoms is 0.06 to 0.50 eV, while the H atoms lose approximately 0.6 eV. The number of electrons gained by the O atoms varies in different intermediates. In *O intermediates, it gains the most electrons, with a range of 0.92 to 1.18 eV. In *OH intermediates, the range is 0.41 to 0.82 eV. In *OOH, each of the two O atoms gains an average of around 0.5 eV of electrons.

Table S13. The d band center ((ε_d, eV) of TM in TM@$PtSe_2$ systems, where Spin up and Spin down are the d band center of spin-up and spin-down electrons, and the average stands for the mean of the total d band center value.

TM	Spin up	Spin down	Average
Ti$^{\times}$	0.071	1.056	0.564
Ti$^{\bullet}$	0.001	1.190	0.596
Ti$^{\bullet\bullet}$	-0.309	0.747	0.219
V$^{\times}$	-0.347	1.846	0.750
V$^{\bullet}$	-0.642	1.047	0.203
V$^{\bullet\bullet}$	-0.651	1.536	0.443
Cr$^{\times}$	-1.294	1.835	0.271
Cr$^{\bullet}$	-1.185	2.151	0.483
Mn$^{\times}$	-2.907	0.657	-1.125
Mn$^{\bullet}$	-2.942	0.694	-1.124
Mn$^{\bullet\bullet}$	0.267	-3.292	-1.513
Fe$^{\times}$	0.192	-2.179	-0.994
Fe$^{\bullet}$	-2.677	0.085	-1.296
Co$^{\times}$	-1.666	-0.457	-1.062
Co$^{\bullet}$	-1.969	-0.371	-1.170
Ni$^{\times}$	-1.295	-1.294	-1.295
Ni$^{\bullet}$	-0.873	-1.257	-1.065
Cu$^{\times}$	-2.504	-2.506	-2.505
Cu$^{\bullet}$	-2.769	-2.768	-2.769
Ru$^{\times}$	-1.672	-1.026	-1.349
Ru$^{\bullet}$	-1.491	-1.251	-1.371
Ru$^{\bullet\bullet}$	-1.170	-1.171	-1.171
Rh$^{\times}$	-1.806	-0.713	-1.260
Rh$^{\bullet}$	-1.831	-1.303	-1.567
Rh′	-1.429	-1.429	-1.429
Pd$^{\times}$	-2.139	-2.140	-2.140
Pd$^{\bullet}$	-1.540	-1.270	-1.405
Ag$^{\times}$	-4.035	-4.035	-4.035

Ag•	-3.534	-3.534	-3.534

Table S14. The PBE (without solvation) and PBE+SOL (with solvation) methods calculate the total magnetic moment (in μ_B) for the oxygenated intermediates before (μ_{B0}) and after adsorbing($\mu_{B\text{-}OH}$, $\mu_{B\text{-}O}$, and $\mu_{B\text{-}OOH}$) on TM@$PtSe_2$.

	PBE				PBE+SOL			
TM	μ_{B0}	$\mu_{B\text{-}OH}$	$\mu_{B\text{-}O}$	$\mu_{B\text{-}OOH}$	μ_{B0}	$\mu_{B\text{-}OH}$	$\mu_{B\text{-}O}$	$\mu_{B\text{-}OOH}$
Ti×	4.00	3.00	2.00	3.00	4.00	3.00	2.00	3.00
Ti•	3.00	2.00	1.00	2.00	3.00	2.00	1.00	2.00
Ti••	3.00	1.00	0.00	1.00	3.00	1.00	0.00	1.00
V×	3.00	2.00	3.00	2.00	3.00	2.00	3.00	2.00
V•	2.00	3.00	2.00	1.00	2.00	3.00	2.00	1.00
V••	3.00	2.00	1.00	2.00	3.00	2.00	1.00	2.00
Cr×	4.00	5.00	2.00	3.00	4.00	5.00	2.00	3.00
Cr•	5.00	4.00	3.00	4.00	5.00	4.00	3.00	4.00
Mn×	5.00	4.00	1.00	4.00	4.74	4.00	1.00	4.00
Mn•	-4.81	5.00	0.00	1.00	-5.83	5.00	0.00	1.00
Mn••	5.00	4.28	1.00	4.00	5.00	4.10	1.00	4.00
Fe×	-2.00	3.00	2.00	4.00	-2.00	3.00	2.00	4.00
Fe•	3.00	4.00	3.00	3.00	3.00	4.00	3.00	3.00
Co×	1.00	2.00	3.00	2.00	1.00	2.00	3.00	2.00
Co•	2.00	3.00	2.00	3.00	2.00	3.00	2.00	3.00
Ni×	0.00	1.00	2.00	1.00	0.00	1.00	2.00	1.00
Ni•	1.00	-2.00	3.00	-2.00	1.00	-2.00	3.00	-2.00
Cu×	0.01	0.00	-1.00	0.00	0.00	0.00	-1.00	0.00
Cu•	0.00	0.98	-2.00	0.98	0.00	0.94	-2.00	1.00
Ru×	2.00	1.00	2.00	1.00	2.00	1.00	2.00	1.00
Ru•	1.00	1.98	1.00	0.00	1.00	1.99	1.00	0.00
Ru••	0.00	1.00	0.00	1.00	0.00	1.00	0.00	1.00
Rh×	1.00	0.00	3.00	0.00	1.00	0.00	3.00	0.00
Rh•	2.00	1.00	2.00	1.00	2.00	1.00	2.00	1.00
Rh′	0.00	0.99	2.00	0.87	0.00	0.99	2.00	0.92
Pd×	0.00	1.00	2.00	1.00	0.00	1.00	2.00	1.00
Pd•	1.00	1.99	3.00	0.00	1.00	1.99	3.00	0.00
Ag×	0.10	0.00	1.00	0.00	0.00	0.00	1.00	0.00
Ag•	0.00	0.42	1.84	0.71	0.00	0.00	1.82	0.94

According to the data in the table, defect charges significantly impact the system's magnetic moment. Different charge states affect the system differently, resulting in varying influences on charge transfer.

Table S15. The descriptors related to structure and atomic properties, including the bond length of TM and coordination atoms ($d_{TM\text{-}Se1}$, $d_{TM\text{-}Se2}$ and $d_{TM\text{-}Se3}$, Å), the d-band center (ε_d, eV), the charge transfer of TM atoms (Q_e, e^-), the electronegativity (N_m), the electron affinity (χ_m, eV), the first ionization energy (I_m, eV), the radius of TM atom (r_d, pm) and the number of TM-d electrons (N_e).

TM	$d_{TM\text{-}Se1}$	$d_{TM\text{-}Se2}$	$d_{TM\text{-}Se3}$	ε_d	Q_e	N_m	χ_m	I_m	r_d	*Ne*
$Ti^{\times}$	2.54	2.54	2.54	0.56	-1.08	1.54	0.08	6.83	146	2
$Ti^{\bullet}$	2.56	2.54	2.56	0. 06	-1.15	1.54	0.08	6.83	146	2
$Ti^{\bullet\bullet}$	2.58	2.57	2.58	0.22	-1.19	1.54	0.08	6.83	146	2
$V^{\times}$	2.46	2.58	2.58	0.75	-0.98	1.63	0.53	6.75	135	3
$V^{\bullet}$	2.48	2.57	2.57	0.20	-1.05	1.63	0.53	6.75	135	3
$V^{\bullet\bullet}$	2.57	2.57	2.57	0.44	-1.03	1.63	0.53	6.75	135	3
$Cr^{\times}$	2.41	2.72	2.72	0.27	-0.83	1.66	0.67	6.77	128	5
$Cr^{\bullet}$	2.62	2.63	2.63	0.48	-0.79	1.66	0.67	6.77	128	5
$Mn^{\times}$	2.60	2.70	2.64	-1.13	-0.67	1.55	-0.50	7.43	126	5
$Mn^{\bullet}$	2.73	2.74	2.74	-1.12	-0.73	1.55	-0.50	7.43	126	5
$Mn^{\bullet\bullet}$	2.74	2.74	2.74	-1.51	-0.92	1.55	-0.50	7.43	126	5
$Fe^{\times}$	2.33	2.46	2.46	-0.99	-0.59	1.83	0.15	7.90	127	6
$Fe^{\bullet}$	2.40	2.56	2.57	-1.30	-0.69	1.83	0.15	7.90	127	6
$Co^{\times}$	2.33	2.33	2.32	-1.06	-0.40	1.88	0.66	7.88	125	7
$Co^{\bullet}$	2.41	2.42	2.42	-1.17	-0.49	1.88	0.66	7.88	125	7
$Ni^{\times}$	2.33	2.33	2.33	-1.30	-0.28	1.91	1.16	7.64	125	8
$Ni^{\bullet}$	2.38	2.38	2.38	-1.07	-0.39	1.91	1.16	7.64	125	8
$Cu^{\times}$	2.46	2.46	2.46	-2.51	-0.32	1.90	1.24	7.73	128	10
$Cu^{\bullet}$	2.45	2.46	2.46	-2.77	-0.42	1.90	1.24	7.73	128	10
$Ru^{\times}$	2.34	2.45	2.45	-1.35	-1.25	2.20	1.05	7.36	134	7
$Ru^{\bullet}$	2.33	2.42	2.44	-1.37	-1.28	2.20	1.05	7.36	134	7
$Ru^{\bullet\bullet}$	2.34	2.39	2.39	-1.17	-1.30	2.20	1.05	7.36	134	6
$Rh^{\times}$	2.41	2.45	2.45	-1.26	-1.10	2.28	1.14	7.46	135	8
$Rh^{\bullet}$	2.45	2.46	2.46	-1.57	-1.20	2.28	1.14	7.46	135	8
Rh'	2.41	2.42	2.42	-1.43	-1.01	2.28	1.14	7.46	135	8
$Pd^{\times}$	2.53	2.54	2.55	-2.14	-1.09	2.20	0.56	8.34	138	8
$Pd^{\bullet}$	2.53	2.54	2.55	-1.41	-1.16	2.20	0.56	8.34	138	7
$Ag^{\times}$	2.75	2.77	2.78	-4.04	-1.24	1.93	1.30	7.58	145	10
$Ag^{\bullet}$	2.74	2.75	2.77	-3.53	-1.37	1.93	1.30	7.58	145	10

Reference

1. C. G. Van de Walle and J. Neugebauer, *J. Appl. Phys.*, 2004, **95**, 3851-3879.
2. S. B. Zhang and J. E. Northrup, *Phys. Rev. Lett.*, 1991, **67**, 2339-2342.
3. S. Lany and A. Zunger, *Phys. Rev. B*, 2008, **78**, 235104.
4. A. Singh and A. K. Singh, *Phys. Rev. Mater.*, 2021, **5**, 084001.
5. A. V. Kuklin, L. V. Begunovich, L. Gao, H. Zhang and H. Ågren, *Phys. Rev. B*, 2021, **104**, 134109.
6. A. Singh and A. K. Singh, *Phys. Rev. B*, 2019, **99**, 121201(R).
7. A. Manjanath, C.-P. Hsu and Y. Kawazoe, *2D Materials*, 2020, **7**, 045024.
8. A. Singh, A. Manjanath and A. K. Singh, *J. Phys. Chem. C*, 2018, **122**, 24475-24480.
9. J.-Y. Noh, H. Kim and Y.-S. Kim, *Phys. Rev. B*, 2014, **89**, 205417
10. J. Zhang, D. Li, L. Ju, G. Yang, D. Yuan, Z. Feng and W. Wang, *Phys. Chem. Chem. Phys.*, 2023, **25**, 10956-10965.
11. W. P. Davey, *Phys. Rev.*, 1925, **25**, 753-761.
12. P. Cherin and P. Unger, *Acta Crystallographica Section B Structural Crystallography and Crystal Chemistry*, 1972, **28**, 313-317.
13. W. J. Yin, S. H. Wei, M. M. Al-Jassim, J. Turner and Y. F. Yan, *Phys. Rev. B*, 2011, **83**, 155102.
14. J. Zhang, X. Chen, M. Deng, H. Shen, H. Li and J. Ding, *Phys. Chem. Chem. Phys.*, 2020, **22**, 25297-25305.
15. J. Zhang, P. Deng, M. Deng, H. Shen, Z. Feng and H. Li, *ACS Omega*, 2020, **5**, 29081-29091.
16. S. Kirklin, J. E. Saal, B. Meredig, A. Thompson, J. W. Doak, M. Aykol, S. Rühl and C. Wolverton, *npj Comput. Mater.*, 2015, **1**, 15010.
17. J. E. Saal, S. Kirklin, M. Aykol, B. Meredig and C. Wolverton, *JOM*, 2013, **65**, 1501-1509.
18. J. H. Friedman, *Annals of statistics*, 2001, **29**, 1189-1232.
19. J. H. Friedman, *Comput. Stat. Data Anal.*, 2002, **38**, 367-378.
20. J. Quinonero-Candela and C. E. Rasmussen, *J. Mach. Learn. Res.*, 2005, **6**, 1939-1959.
21. A. Liaw and M. Wiener, *R news*, 2002, **2**, 18-22.
22. A. Seko, T. Maekawa, K. Tsuda and I. Tanaka, *Phys. Rev. B*, 2014, **89**, 054303.
23. J.-C. Wu, J. Zheng, P. Wu and R. Xu, *J. Phys. Chem. C*, 2011, **115**, 5675-5682.
24. Y. Wang, L. Li, W. Yao, S. Song, J. T. Sun, J. Pan, X. Ren, C. Li, E. Okunishi, Y. Q. Wang, E. Wang, Y. Shao, Y. Y. Zhang, H. T. Yang, E. F. Schwier, H. Iwasawa, K. Shimada, M. Taniguchi, Z. Cheng, S. Zhou, S. Du, S. J. Pennycook, S. T. Pantelides and H. J. Gao, *Nano Lett.*, 2015, **15**, 4013-4018.
25. F. Ghasemi, R. Taghavimendi and A. Bakhshayeshi, *Optical and Quantum Electronics*, 2020, **52**, 1-14.
26. P. Li, L. Li and X. C. Zeng, *J. Mater. Chem. C*, 2016, **4**, 3106-3112.
27. H. L. Zhuang and R. G. Hennig, *J. Phys. Chem. C*, 2013, **117**, 20440-20445.
28. J. Li, S. Kolekar, M. Ghorbani-Asl, T. Lehnert, J. Biskupek, U. Kaiser, A. V. Krasheninnikov and M. Batzill, *ACS nano*, 2021, **15**, 13249-13259.
29. J. Rossmeisl, Z. W. Qu, H. Zhu, G. J. Kroes and J. K. Nørskov, *J. Electroanal. Chem.*, 2007, **607**, 83-89.
30. M. T. Li, L. P. Zhang, Q. Xu, J. B. Niu and Z. H. Xia, *J. Catal.*, 2014, **314**, 66-72.
31. E. Fabbri, A. Habereder, K. Waltar, R. Kötz and T. J. Schmidt, *Catal. Sci. Technol.*, 2014, **4**, 3800-3821.

32. V. Tripkovic, E. Skulason, S. Siahrostami, J. K. Norskov and J. Rossmeisl, *Electrochim. Acta*, 2010, **55**, 7975-7981.
33. X. Liu, Y. Zhang, W. Wang, Y. Chen, W. Xiao, T. Liu, Z. Zhong, Z. Luo, Z. Ding and Z. Zhang, *ACS Appl. Mater. Interfaces*, 2022, **14**, 1249-1259.
34. H. Niu, X. Wan, X. Wang, C. Shao, J. Robertson, Z. Zhang and Y. Guo, *ACS Sustainable Chem. Eng.*, 2021, **9**, 3590-3599.
35. H. Niu, X. Wang, C. Shao, Y. Liu, Z. Zhang and Y. Guo, *J. Mater. Chem. A*, 2020, **8**, 6555-6563.
36. X. Wang, H. Niu, X. Wan, J. Wang, C. Kuai, Z. Zhang and Y. Guo, *Appl. Surf. Sci.*, 2022, **582**, 152470.
37. W. Yao, Y. Qu, M. Zhou, W. Wang, A. Zhang, Z. Feng and H. Yan, *Mol. Catal.*, 2024, **554**, 113807.
38. I. Yamada, A. Takamatsu, K. Asai, T. Shirakawa, H. Ohzuku, A. Seno, T. Uchimura, H. Fujii, S. Kawaguchi, K. Wada, H. Ikeno and S. Yagi, *J. Phys. Chem. C*, 2018, **122**, 27885-27892.
39. Q. Liu, X. Zhao and X. Chen, *J. Colloid Interface Sci.*, 2023, **648**, 787-797.
40. H. ROHDE and H. KUDIELKA, *Zeitschrift für Kristallographie-Crystalline Materials*, 1960, **114**, 447-456.
41. V. Goldschmidt, *Naturwissenschaften*, 1930, **18**, 999-1013.
42. M. Knecht, H. Ebert and W. Bensch, *J. Alloys Compd.*, 1997, **246**, 166-176.
43. K. Hayashi and M. Nakahira, *J. Solid State Chem.*, 1978, **24**, 153-161.
44. A. Kallel and H. Boller, *Journal of the Less Common Metals*, 1984, **102**, 213-217.
45. A. Galyas and G. Makovetskii, *Cryst. Res. Technol.*, 1985, **20**, 819-826.
46. C. Van Bruggen, R. Haange, G. Wiegers and D. De Boer, *Physica B+ c*, 1980, **99**, 166-172.
47. F. Wehmeier, E. Keve and S. Abrahams, *Inorg. Chem.*, 1970, **9**, 2125-2131.
48. L. Cemic and A. Neuhaus, *High Temp—High Press*, 1972, **4**, 97-99.
49. J. Hastings, N. Elliott and L. Corliss, *Phys. Rev.*, 1959, **115**, 13.
50. M. Shivastava and O. Srivastava, *Thin Solid Films*, 1975, **29**, 275-284.
51. A. Kjekshus, T. Rakke and A. AF, *Acta Chem. Scand. A* 1974, **28a**, 996-1000.
52. A. Andresen and B. VANLAAR, *Acta Chem. Scand.*, 1970, **24**, 2435-2439.
53. V. K. Dalal, H. Keer and A. Biswas, *J. Inorg. Nucl. Chem.*, 1971, **33**, 2839-2845.
54. P. Ramdohr and M. Schmitt, *Neues Jahrb. Mineral., Monatsh*, 1955, **6**, 133-142.
55. F. J. García-García, A.-K. Larsson, L. Norèn and R. L. Withers, *Solid State Sci.*, 2004, **6**, 725-733.
56. A. Singh, M. Srivastava and O. Srivastava, *Journal of the Less Common Metals*, 1978, **57**, 225-227.
57. H. Haraldsen, R. Mollerud and E. Rost, *Acta Chem. Scand.*, 1967, **21**, 1727-1736.
58. T. Connolly, in *Groups IV, V, and VI Transition Metals and Compounds: Preparation and Properties*, Springer, 1972, pp. 179-197.
59. V. Milman, *Acta Crystallogr. Sect. B: Struct. Sci.*, 2002, **58**, 437-447.
60. N. Morimoto and K. Koto, *Science*, 1966, **152**, 345-345.
61. L. Thomassen, *Z. Phys. Chem.*, 1929, **2**, 349-379.
62. T. Rummery and R. Heyding, *Can. J. Chem.*, 1967, **45**, 131-137.
63. K. Schubert, H. Breimer, W. Burkhardt, E. Günzel, R. Haufler, H. Lukas, H. Vetter, J. Wegst and M. Wilkens, *Naturwissenschaften*, 1957, **44**, 229-230.
64. F. Grønvold and E. Røst, *Acta Crystallogr.*, 1957, **10**, 329-331.

65. I. Nuriev, R. Imamov and R. Shafizade, *Kristallografiya*, 1971, **16**, 1028-1030.
66. H. Billetter and U. Ruschewitz, *Z. Anorg. Allg. Chem.*, 2008, **634**, 241-246.
67. S. Kirklin, J. E. Saal, B. Meredig, A. Thompson, J. W. Doak, M. Aykol, S. Rühl and C. Wolverton, *npj Comput. Mater.*, 2015, **1**, 1-15.
68. K. Mathew, R. Sundararaman, K. Letchworth-Weaver, T. A. Arias and R. G. Hennig, *J. Chem. Phys.*, 2014, **140**, 084106.
69. M. Prabu, K. Ketpang and S. Shanmugam, *Nanoscale*, 2014, **6**, 3173-3181.
70. Y. Yu, J. Zhou and Z. Sun, *Adv. Funct. Mater.*, 2020, **30**, 2000570.
71. J. Wang, Y. Fan, S. Qi, W. Li and M. Zhao, *J. Phys. Chem. C*, 2020, **124**, 9350-9359.
72. C. Y. Lin, L. Zhang, Z. Zhao and Z. Xia, *Adv. Mater.*, 2017, **29**, 1606635.
73. S. Lu, H. L. Huynh, F. Lou, K. Guo and Z. Yu, *Nanoscale*, 2021, **13**, 12885-12895.
74. S. Lu, Y. Zhang, F. Lou, K. Guo and Z. Yu, *Appl. Surf. Sci.*, 2022, **579**, 152234.
75. Y. Zheng, Y. Jiao, Y. Zhu, Q. Cai, A. Vasileff, L. H. Li, Y. Han, Y. Chen and S. Z. Qiao, *J. Am. Chem. Soc.*, 2017, **139**, 3336-3339.
76. Y. Ying, K. Fan, X. Luo, J. Qiao and H. Huang, *J. Mater. Chem. A*, 2021, **9**, 16860-16867.
77. T. Zhang, B. Zhang, Q. Peng, J. Zhou and Z. Sun, *J. Mater. Chem. A*, 2021, **9**, 433–441.
78. H. Zeng, X. Liu, F. Chen, Z. Chen, X. Fan and W. Lau, *ACS Appl. Mater. Interfaces*, 2020, **12**, 52549-52559.
79. Z. Qin and J. Zhao, *J. Colloid Interface Sci.*, 2022, **605**, 155-162.
80. Q. Deng, J. Han, J. Zhao, G. Chen, T. Vegge and H. Anton Hansen, *J. Catal.*, 2021, **393**, 140-148.
81. Z. Qin, Z. Wang and J. Zhao, *Nanoscale*, 2022, **14**, 6902-6911.
82. Y. Zhou, G. Gao, J. Kang, W. Chu and L.-W. Wang, *J. Mater. Chem. A*, 2019, **7**, 12050-12059.